Detection and attribution of an anomaly in terrestrial photosynthesis in Europe during the COVID-19 lockdown

Angela Che Ing Tang, Christophe Flechard, Nicola Arriga, Dario Papale, Paul C Stoy, Nina Buchmann, Matthias Cuntz, John Douros, Silvano Fares, Alexander Knohl, et al.

Detection and attribution of an anomaly in terrestrial photosynthesis in Europe during the COVID-19 lockdown

Angela Che Ing Tang [a,b,*], Christophe R. Flechard [c], Nicola Arriga [d], Dario Papale [e,f], Paul C. Stoy [g], Nina Buchmann [h], Matthias Cuntz [i], John Douros [j], Silvano Fares [k], Alexander Knohl [l], Ladislav Šigut [m], Guillaume Simioni [n], Renske Timmermans [o], Thomas Grünwald [p], Andreas Ibrom [q], Benjamin Loubet [r], Ivan Mammarella [s], Luca Belelli Marchesini [t], Mats Nilsson [u], Matthias Peichl [u], Corinna Rebmann [v], Marius Schmidt [w], Christian Bernhofer [p], Daniel Berveiller [x], Edoardo Cremonese [y], Tarek S. El-Madany [z], Mana Gharun [h,aa], Damiano Gianelle [t], Lukas Hörtnagl [h], Marilyn Roland [ab], Andrej Varlagin [ac], Zheng Fu [ad], Bernard Heinesch [ae], Ivan Janssens [ab], Natalia Kowalska [m], Jiří Dušek [m], Giacomo Gerosa [af], Meelis Mölder [ag], Eeva-Stiina Tuittila [ah], Denis Loustau [a]

[a] ISPA, Bordeaux Sciences Agro, INRAE, Villenave d'Ornon, France
[b] Department of Environmental Sciences, University of Toledo, Toledo, OH, USA
[c] UMR SAS, INRAE, Institut Agro, Rennes, France
[d] Joint Research Centre, European Commission, Ispra, Italy
[e] University of Tuscia DIBAF, Viterbo, Italy
[f] EuroMediterranean Center on Climate Change, CMCC IAFES, Viterbo, Italy
[g] Department of Biological Systems Engineering, University of Wisconsin-Madison, Madison, WI, USA
[h] Department of Environmental Systems Science, ETH Zurich, Zurich, Switzerland
[i] Université de Lorraine, AgroParisTech, INRAE, UMR Silva, Nancy, France
[j] Royal Netherlands Meteorological Institute (KNMI), De Bilt, The Netherlands
[k] National Research Council of Italy, Institute for Agriculture and Forestry Systems in the Mediterranean, Naples, Italy
[l] Bioclimatology, University of Göttingen, Göttingen, Germany
[m] Department of Matter and Energy Fluxes, Global Change Research Institute of the Czech Academy of Sciences, Brno, Czech Republic
[n] URFM, INRAE, Avignon, France
[o] Climate Air and Sustainability Unit, Netherlands Organisation for Applied Scientific Research (TNO), Utrecht, The Netherlands
[p] Faculty of Environmental Sciences, Institute of Hydrology and Meteorology, Technische Universität Dresden, Tharandt, Germany
[q] Technical University of Denmark (DTU), DTU-Sustain, Kgs. Lyngby, Denmark
[r] UMR ECOSYS, AgroParisTech, INRAE, Université Paris-Saclay, Thiverval-Grignon, France
[s] Institute for Atmospheric and Earth System Research/Physics, University of Helsinki, Helsinki, Finland
[t] Research and Innovation Centre, Fondazione Edmund Mach, San Michele all'Adige, Italy
[u] Department of Forest Ecology and Management, Swedish University of Agricultural Sciences, Umeå, Sweden
[v] Department of Computational Hydrosystems, Helmholtz Centre for Environmental Research – UFZ, Leipzig, Germany
[w] Institute of Bio- and Geosciences: Agrosphere (IBG-3), Jülich Research Centre, Jülich, Germany
[x] Université Paris-Saclay, CNRS, AgroParisTech, Ecologie Systématique et Evolution, Orsay, France
[y] Environmental Protection Agency of Aosta Valley - Climate Change Unit, Saint-Christophe, Italy
[z] Max Planck Institute for Biogeochemistry, Department of Biogeochemical Integration, Jena, Germany
[aa] Faculty of Geosciences, University of Münster, Münster, Germany
[ab] Department of Biology, University of Antwerp, Wilrijk, Belgium
[ac] A.N. Severtsov Institute of Ecology and Evolution, Russian Academy of Sciences, Moscow, Russia
[ad] Laboratoire des Sciences du Climat et de l'Environnement, LSCE/IPSL, CEA-CNRS-UVSQ, Université Paris-Saclay, Gif-sur-Yvette, France
[ae] TERRA Teaching and Research Centre, University of Liege, Gembloux, Belgium
[af] Università Cattolica del Sacro Cuore, Brescia, Italy
[ag] Department of Physical Geography and Ecosystem Science, Lund University, Lund, Sweden
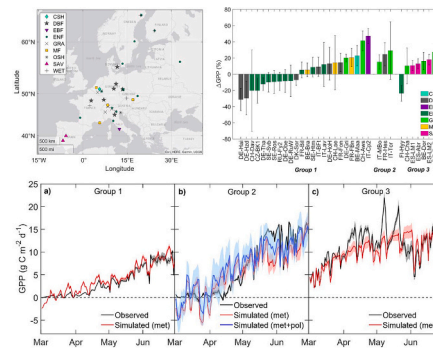[ah] School of Forest Sciences, University of Eastern Finland, Joensuu, Finland

* Corresponding author at: ISPA, Bordeaux Sciences Agro, INRAE, Villenave d'Ornon, France.
E-mail address: tang.angelaci@gmail.com (A.C.I. Tang).

GRAPHICAL ABSTRACT

ARTICLE INFO

ABSTRACT

Carbon dioxide (CO_2) uptake by plant photosynthesis, referred to as gross primary production (GPP) at the ecosystem level, is sensitive to environmental factors, including pollutant exposure, pollutant uptake, and changes in the scattering of solar shortwave irradiance (SW_{in}) – the energy source for photosynthesis. The 2020 spring lockdown due to COVID-19 resulted in improved air quality and atmospheric transparency, providing a unique opportunity to assess the impact of air pollutants on terrestrial ecosystem functioning. However, detecting these effects can be challenging as GPP is influenced by other meteorological drivers and management practices. Based on data collected from 44 European ecosystem-scale CO_2 flux monitoring stations, we observed significant changes in spring GPP at 34 sites during 2020 compared to 2015–2019. Among these, 14 sites showed an increase in GPP associated with higher SW_{in}, 10 sites had lower GPP linked to atmospheric and soil dryness, and seven sites were subjected to management practices. The remaining three sites exhibited varying dynamics, with one experiencing colder and rainier weather resulting in lower GPP, and two showing higher GPP associated with earlier spring melts. Analysis using the regional atmospheric chemical transport model (LOTOS-EUROS) indicated that the ozone (O_3) concentration remained relatively unchanged at the research sites, making it unlikely that O_3 exposure was the dominant factor driving the primary production anomaly. In contrast, SW_{in} increased by 9.4 % at 36 sites, suggesting enhanced GPP possibly due to reduced aerosol optical depth and cloudiness. Our findings indicate that air pollution and cloudiness may weaken the terrestrial carbon sink by up to 16 %. Accurate and continuous ground-based observations are crucial for detecting and attributing subtle changes in terrestrial ecosystem functioning in response to environmental and anthropogenic drivers.

1. Introduction

The emergence of the novel coronavirus disease (COVID-19) in late 2019 and its rapid global spread led to significant restrictions on human activities. Many European countries implemented stringent measures, including full or partial lockdowns, following the World Health Organisation's declaration of Europe as the global epicentre of the pandemic on 13 March 2020 (World Health Organisation, 2020). These lockdown measures entailed the closure of borders, schools and non-essential businesses, along with the implementation of "stay at home" policies and mobility restrictions. Consequently, there was an unprecedented reduction in primary air pollutant emissions across much of Europe.

Specific restrictions varied by country, but during the most intensive lockdown period of lockdown between March 23 and April 26, substantial reductions in emissions were observed. Nitrogen oxides (NO_x) decreased by an average of 33 %, non-methane volatile organic compounds (NMVOCs) by 8 %, sulphur oxides (SO_x) by 7 %, and particulate matter 2.5 ($PM_{2.5}$) by 7 % across 30 European countries (Guevara et al., 2021). Road transport accounted for > 85 % of the total reduction in all pollutants, except for SO_x (Guevara et al., 2021).

The reduction of NO_x emissions resulted in a substantial decrease in nitrogen dioxide (NO_2) concentration, as observed through measurements, modelling and satellite-based data, with reductions ranging from 20 % to 50 % (Barré et al., 2021; Bauwens et al., 2020; Menut et al.,

2020; Putaud et al., 2021). However, the impact of the lockdown on PM concentration was less pronounced, with decreases on the order of 5 % to 15 % depending on region. This difference can be attributed to complex chemical reactions, meteorological variability, unaffected ammonia (NH_3) emissions from business-as-usual agricultural operations, and increases in emission from domestic heating (Menut et al., 2020; Venter et al., 2020).

The impact of lockdown on atmospheric ozone (O_3) concentration – known to reduce leaf level photosynthesis – was mixed. Most urban areas experienced higher-than-usual O_3 concentration due to reduced atmospheric titration by NO, while a slight decrease or increase in O_3 was observed downwind of cities and in rural areas (Menut et al., 2020; Ordóñez et al., 2020). Regional variations in meteorological conditions played a dominant role in the O_3 anomaly. Decreases in O_3 concentration were observed in the Iberian Peninsula, southern and western France, central Italy and some locations of northern Europe, while increases were observed in other areas (Ordóñez et al., 2020).

While the effects of lockdown measures on air pollutant concentrations have been well-documented, there is still a significant gap in our understanding of how terrestrial ecosystems' photosynthetic activity specifically responds to changes in air quality. To better understand the resilience and functioning of terrestrial ecosystems, it is crucial to gain insight into the real-world response of plant productivity, particularly gross primary production (GPP), to variations in air quality. The spring

2020 lockdown's substantial reduction in primary pollutant emissions provides a unique opportunity to assess how improved air quality can affect GPP. Understanding these intricate relationships is essential, as atmospheric pollutants can have diverse effects on plant productivity, both positive and negative, and over different time scales. Particulate matter, for instance, has somewhat counter-intuitively the potential to enhance GPP by allowing more diffuse radiation to penetrate plant canopies (Mercado et al., 2009; Roderick et al., 2001; Wang et al., 2018). On the other hand, O_3 causes direct oxidative damage to the photosynthetic machinery (Grene, 2002; Pell et al., 1997; Wittig et al., 2009). Among atmospheric pollutants, long-term dry and wet deposition of nitrogen (N) can influence GPP both positively (where N is limiting) and negatively (where N saturation occurs) (Flechard et al., 2020a; Flechard et al., 2020b).
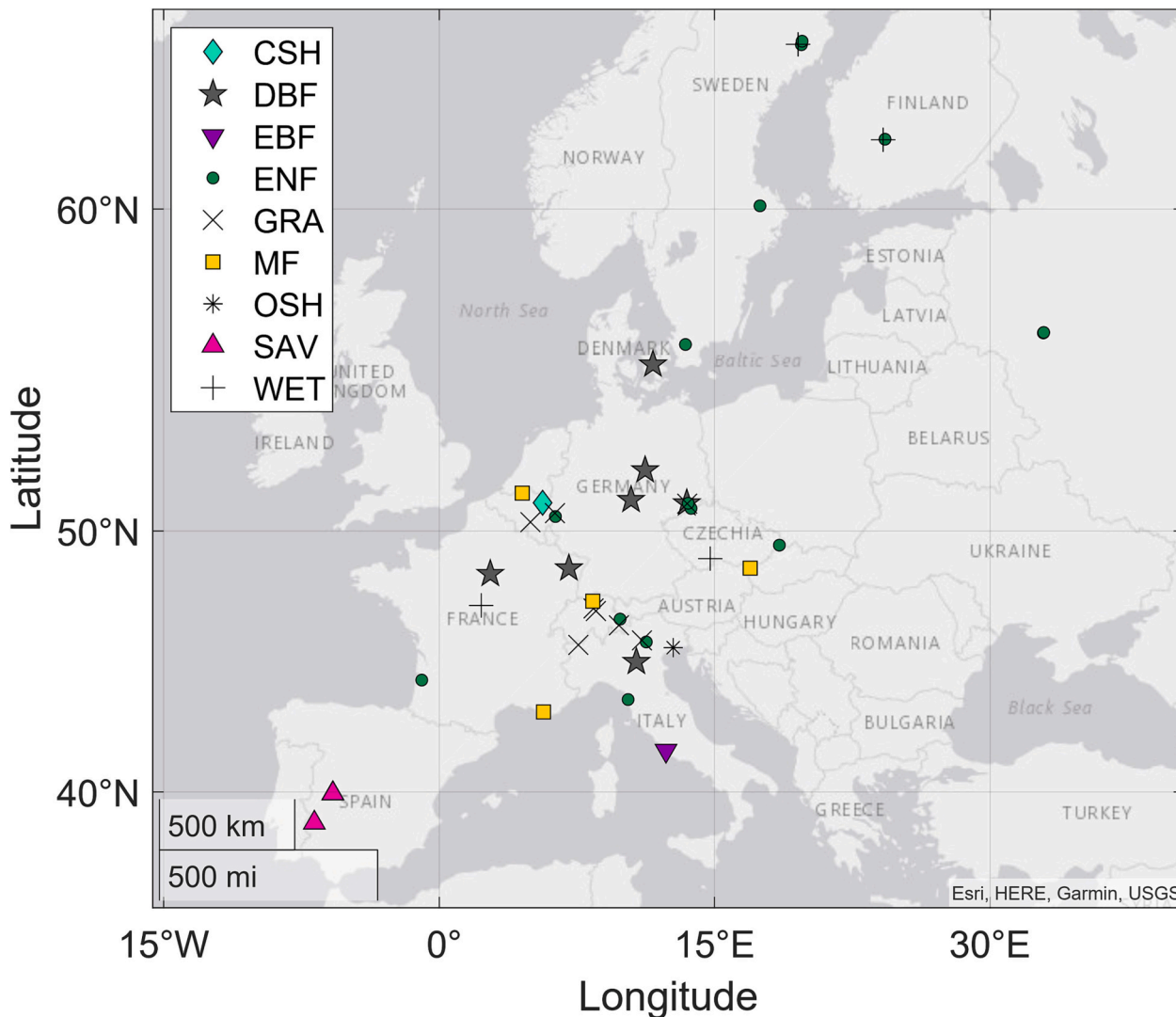
Our study aims to address such knowledge gaps by investigating several hypotheses. Firstly, we aim to demonstrate the effectiveness of a network of ecosystem-scale CO_2 flux monitoring stations in detecting changes in GPP during the COVID-19 lockdown. Secondly, we postulate that GPP during the spring of 2020 was higher due to the reduction of atmospheric pollutants compared to previous years. Thirdly, we anticipate that the decrease in PM concentrations and the subsequent increase in incoming shortwave solar radiation (SW_{in}), and thus in photosynthetically active radiation (PAR) would enhance photosynthesis. Lastly, we hypothesize that the reduction of NO_x emissions would lead to decreased O_3 formation in rural areas and reduced its phytotoxic effects, resulting in increased photosynthesis. To test these hypotheses, we analysed turbulent surface-atmosphere CO_2 fluxes from eddy covariance measurements and meteorological data from 44 ecosystem monitoring stations across Europe, alongside air pollution data simulated by a regional-scale chemical transport model (LOTOS-EUROS). This study represents the first assessment of the potential impacts of COVID-19 lockdowns on terrestrial ecosystem GPP, contributing to a better understanding of the interactions between air quality, environmental factors and ecosystem productivity.

2. Materials and methods

2.1. Fluxes and meteorological datasets

This analysis utilized eddy covariance fluxes and meteorological data collected at the 44 European ecosystem flux tower stations (Fig. 1), which can be accessed through the Integrated Carbon Observation System (ICOS) Carbon Portal (Warm Winter 2020 Team and ICOS Ecosystem Thematic Centre, 2022). These stations are located in 11 European countries and represent nine plant functional types, including closed shrubland (CSH), deciduous broadleaf forest (DBF), evergreen

Fig. 1. Location of the 44 eddy covariance flux tower sites in this study. Abbreviations: CSH, closed shrubland; DBF, deciduous broadleaf forest; EBF, evergreen broadleaf forest; ENF, evergreen needleleaf forest; GRA, grassland; MF, mixed forest; OSH, open shrubland; SAV, savannah; WET, wetland.

broadleaf forest (EBF), evergreen needleleaf forest (ENF), grassland (GRA), mixed forest (MF), open shrubland (OSH), savannah (SAV) and wetland (WET). The dataset thus covers the main European geographical areas, and the dominant plant functional types present in Europe, with the exception of croplands, which were excluded from the analysis due to the year-to-year variability in crops within pluri-annual rotations, making the detection of GPP anomalies difficult to discern.

The majority of our study sites are located in rural areas. However, several peri-urban sites are also included, located in close proximity to major European metropolitan areas. These include FR-Fon, situated 50 km from Paris (with a metropolitan population of 13 million inhabitants); IT-Cp2, located 25 km from Rome (with a population of 4.3 million inhabitants); CH-Cha, CH-Fru and CH-Lae, all within 30 km from Zürich (with a population of 1.4 million inhabitants); DE-Gri, DE-Hzd, DE-Obe and DE-Tha, all located within 30 km from Dresden (with a population of 1.3 million inhabitants); and BE-Bra, situated 13 km from Antwerp (with a population of 1.1 million inhabitants).

The CO_2 flux data used in this study were subjected to quality control and processed using standardized procedures described in Pastorello et al. (2020). At each site, net ecosystem CO_2 exchange (NEE) was filtered using 40 different friction velocity thresholds and gaps in the half-hourly data were filled, resulting in 40 alternative full time-series of NEE. The most representative NEE values were selected based on the Nash-Sutcliffe model efficiency coefficient (Pastorello et al., 2020). GPP and ecosystem respiration (TER) were derived using daytime and nighttime partitioning methods (Lasslop et al., 2010; Reichstein et al., 2005). To avoid any potential circularity issues with light response parameter estimations (see Section 2.6), we used GPP estimates that were calculated using the temperature response function of TER from measured nighttime NEE (Reichstein et al., 2012). The uncertainty of NEE was quantified as the joint uncertainty, which includes both random uncertainty (Hollinger and Richardson, 2005) and the uncertainty associated with friction velocity thresholds (Pastorello et al., 2020). To calculate uncertainty in GPP and TER, only the uncertainty associated with friction velocity thresholds was retained, using the 25th and 75th percentile values of the ensemble generated with 40 friction velocity thresholds. The uncertainty was then summed over the period considered. In this study, we defined the reference period as the springtime interval from March to June in the years 2015–2019 for several reasons. Firstly, most sites have observational data since 2015, and this period is recent enough to be representative of conditions in 2020, both in terms of climate and vegetation characteristics. Secondly, using a medium-term averaging period increases the likelihood of obtaining a 'normal' approximation, which can help to even out short-term swings induced by interannual meteorological variability. The reference period is defined as the average across the years 2015–2019 or specific years for certain sites as listed in Table S1 and described below.

To ensure high quality data for bias-free comparison and analysis, we further screened the four-month gap-filled NEE data of each year that were available between 2015 and 2020 based on quality flags. Quality flags of 0, 1, 2 and 3 indicate measured fluxes, good quality, medium quality and poor quality gap-filled NEE, respectively (Pastorello et al., 2020). Specifically, we only included the spring data in which at least 80 % of the NEE data had quality flags of 0 to 2. This screening process resulted in a total of 44 sites for this study, with 31 sites providing data for the full study period of 2015–2020 (i.e. six years), 10 sites providing five years of data, two sites providing four years of data, and one site providing two-year of data (Table S1).

2.2. Air pollution datasets

To determine ecosystem exposure to atmospheric pollution, we used hourly air pollutant concentration data simulated by a regional-scale chemical transport model (LOTOS-EUROS) (Manders-Groot et al., 2016), which had a spatial resolution of $0.1° \times 0.1°$. The simulated pollutants included gaseous species such as ozone (O_3), nitrogen dioxide

(NO_2), nitric oxide (NO), ammonia (NH_3) and sulphur dioxide (SO_2), as well as particulate matter (PM), which consisted of secondary inorganic aerosol smaller than 2.5 μm ($SIA_{2.5}$), particulate matter smaller than 10 μm (PM_{10}) and particulate matter smaller than 2.5 μm ($PM_{2.5}$). The LOTOS-EUROS model has various sources of uncertainties related to its different components such as emissions, chemical conversions, chemical interactions between species, and deposition (Manders et al., 2017). These uncertainties can lead to different behaviours for each modelled species, making it difficult to accurately predict their concentrations in the atmosphere. To verify the model, we conducted a comparison between the measured and modelled half-hourly averaged O_3 concentrations at the FI-Hyy site, where on-site ozone measurements were available, during the reference and lockdown periods in 2020. The results showed reasonable agreement between the measured and modelled data (Fig. S1).

To quantify the relative change in pollutant concentrations between the reference period and the year 2020, two calculations were performed: one with "business as usual" emissions, i.e. no COVID-19 reductions were considered, and another with COVID-19 modulated anthropogenic emissions (Guevara et al., 2021). For short vegetation sites (CSH, GRA, OSH, SAV and WET), we used ground level air pollutant concentrations (~2 m above the surface), while for forests (DBF, EBF, ENF and MF), we used the concentration at 12.5 m (i.e. within or just above the tree canopy). To obtain half-hourly estimates from the series of hourly concentration that were consistent with the data acquisition frequency for fluxes and meteorological data, we applied a linear interpolation procedure to the series of hourly concentration.

2.3. Diffuse and total radiation

To compensate for the lack of full radiation instruments at some study sites, we utilized solar radiation components (global SW_{in}, direct SW_{dir} and diffuse SW_{dif}) from the Copernicus Atmosphere Monitoring Service (CAMS) radiation service. These data were obtained at 15-min intervals for all- and clear-sky conditions (Gschwind et al., 2019; Lefèvre et al., 2013; Qu et al., 2017). UTC date and time were converted to the local time, and half-hourly irradiance data were calculated by averaging the 15-min measurements. The diffuse radiation fraction (DF) was then determined as the ratio of diffuse to global irradiance on the horizontal plane at ground level. Both the CAMS all-sky and clear-sky radiation estimates were subjected to rigorous input quality control, regular benchmarking against ground stations, and regular monitoring to ensure consistency and detect possible trends (Schroedter-Homscheidt et al., 2021).

The mean bias between the on-site measurements and CAMS data was found to be 2.3 ± 7.2 W m^{-2}, indicating a good agreement between the measured and modelled SW_{in}. Additionally, we compared the CAMS modelled SW_{dif} with the on-site measurements at a deciduous broadleaf forest site in Germany (DE-HoH). The temporal analysis demonstrated a high degree of agreement between the observed and modelled data throughout the 2015–2020 period (Fig. S2). These findings further validate the reliability and accuracy of the CAMS radiation service in estimating solar radiation parameters.

2.4. Quantification of spring 2020 anomalies

To quantify potential anomalies for spring 2020 (March–April–May–June), we compared the variables in 2020 (X_{2020}) to the reference period from 2015 to 2019 (X_{ref}). For each of the variables GPP, NEE, TER, precipitation (P_{tot}) and evapotranspiration (ET), we calculated the average spring sum over the reference period. For all other variables, we calculated the mean for each period from half-hourly data and averaged them for the reference period. We then expressed the anomalies as both absolute (ΔX) and relative (ΔY) changes using the following equations:

$$\Delta X = X_{2020} - X_{ref} \tag{1}$$

and

$$\Delta Y = \frac{X_{2020} - X_{ref}}{X_{ref}} \times 100\% \tag{2}$$

A positive anomaly indicates that X was higher during the 2020 spring than during the reference period.

2.5. Statistical analysis

To assess the statistical significance of the differences between the reference period and the 2020 data, we used the Student's t-test to test the null hypothesis that the difference between the mean of 2015–2019 and 2020 is zero at the 5 % significance level.

2.6. Maximal rate of photosynthesis and canopy radiation-use efficiency

We estimated the ecosystem light response parameter (α, γ, P_{max}) by fitting the Michaelis-Menten rectangular hyperbola function (Falge et al., 2001; Lasslop et al., 2010) to measured half-hourly NEE data from April 20 to May 15 as follows:

$$NEE = -\frac{\alpha P_{max} SW_{in}}{\alpha SW_{in} + P_{max}} + \gamma \tag{3}$$

Here, NEE (μmol m^{-2} s^{-1}) is the net ecosystem CO$_2$ exchange, α (μmol CO$_2$ J^{-1}) represents the initial slope of the light-response curve (also known as the canopy radiation-use efficiency), P_{max} (μmol CO$_2$ m^{-2} s^{-1}) denotes the maximum canopy CO$_2$ uptake rate at light saturation, γ (μmol CO$_2$ m^{-2} s^{-1}) is ecosystem respiration (TER), and SW$_{in}$ (W m^{-2}) is the incoming shortwave radiation. To mitigate the potential influence of substantial changes in leaf area index (LAI) from March to June, particularly at colder weather sites, we specifically selected the period from April 20 to May 15 to estimate the ecosystem light response parameters. Additionally, we only included data with vapour pressure deficit (VPD) values below 1.5 kPa to avoid the confounding effect of VPD limitation on canopy conductance and photosynthesis.

2.7. Multiple linear model and simulation

To investigate the causes of the spring 2020 GPP anomalies, we constructed multivariate models based on data for potential environmental drivers from the reference period and compared the simulated estimates to observed values. Using meteorological variables (SW$_{in}$, SW$_{dif}$, T$_a$ and VPD) obtained at each site, we built a multivariate model of GPP with a least square regression. We identified the most parsimonious linear model of GPP by applying information criterion techniques via the dredge function of the "MuMIn" package in R (Bartoń, 2020; Tang et al., 2018). The dredge algorithm generates all possible univariate and multivariate models of the response variable (GPP) based on predictors (meteorological and/or pollutant variables), and selects the model with the minimum value of the Akaike information criterion (AIC) – the model with the lowest value of the likelihood function by number of model parameters – as the most parsimonious (Akaike, 1976). We then used this model trained on the reference period to predict the 2020 GPP at a daily time scale. In addition to R^2, we used the normalized root-mean-square error (NRMSE) values computed by the MATLAB "compare" function to assess the model's fitness by indicating how well the predictions or simulations matched the observed data (MathWorks, 2022). The NRMSE ranges from $-\infty$ to 100 %, where 100 % indicates a perfect fit, $-\infty$ indicates a poor fit and a fitness value of zero indicates that the identified model is no better than a straight line at matching the observed output.

3. Results

3.1. GPP, meteorological and air pollution anomalies during the spring 2020 lockdown

The spring GPP anomaly for 2020, ΔGPP, varied widely among the 44 sites, ranging from -202 to $+390$ g C m^{-2} (-31 % to $+47$ %) (Fig. S3). Overall, we observed an increase in both the mean GPP and its standard deviation ($+5.3$ % or $+39$ g C m^{-2}, $p = .04$, and $+18$ %, respectively) (Fig. 2). Notably, among the 44 sites, 34 sites showed significant differences between the 2020 and reference GPP at the 5 % level. Of these 34 sites, 22 sites showed a positive anomaly ranging from $+5.2$ % to $+47$ %, while 12 sites showed a negative anomaly of -7.1 % to -47 % (Fig. S1, Table S1). We found no marked differences in GPP, meteorological conditions and pollutant anomalies between peri-urban sites and other sites (Tables S1, S2 and S3). Consequently, all sites were pooled together in the analysis.

Fig. 3 illustrates the difference in the frequency distribution of GPP and its drivers between the spring 2020 and the reference period across the 44 sites. During the spring of 2020, the distribution of GPP shifted towards higher values, coinciding with clearer and drier atmospheric conditions. The average increase in SW$_{in}$ in 2020 was $+13 \pm 13$ W m^{-2} (mean $\pm$ SD, a relative change of $+6.9$ %, $p < .001$) for the measured SW$_{in}$ and $+11 \pm 9$ W m^{-2} ($+5.6$ %, $p < .001$) for the CAMS modelled SW$_{in}$, respectively, across all sites (Table S2). Specifically, there were increases in SW$_{dir}$ ($+13 \pm 12$ W m^{-2}, $+12$ %, $p < .001$), as well as reductions in SW$_{dif}$ (-2.4 ± 4 W m^{-2}, -2.8 %, $p < .001$) and the diffuse radiation fraction (DF) (-0.04 ± 0.04, -6.4 %, $p < .001$).

The ambient concentrations of several air pollutants, simulated by the LOTOS-EUROS model, declined significantly in spring 2020 ($p < .001$) for each species: NO by -0.08 ± 0.09 ppb (-32 %), NO$_2$ by -0.48 ± 0.49 ppb (-26 %), SIA$_{2.5}$ by -0.64 ± 0.53 μg m^{-3} (-18 %), PM$_{2.5}$ by -0.71 ± 0.58 μg m^{-3} (-12 %), PM$_{10}$ by -0.77 ± 0.61 μg m^{-3} (-7.8 %), and SO$_2$ by -0.01 ± 0.01 ppb (-4.5 %). However, despite substantial reductions in its precursors, there was a small but still significant anomaly of O$_3$ concentration (-0.72 ± 0.51 ppb, -1.8 %, $p < .001$). In contrast, atmospheric NH$_3$, which is emitted primarily from agricultural activities such as manure and fertilizer application in spring, remained relatively stable with a minor increase of $+1.35$ % ($+0.07 \pm 0.07$ ppb, $p < .001$).

We analysed the cumulative GPP and environmental variables averaged over the 44 sites in spring 2020 and compared them with each previous spring from 2015 to 2019 (Table 1). Our results show that the GPP increased by $+44 \pm 178$ g C m^{-2} ($+5.7$ %), $+35 \pm 144$ g C m^{-2} ($+4.9$ %), $+62 \pm 129$ g C m^{-2} ($+8.9$ %) and $+43 \pm 137$ g C m^{-2} ($+6.1$ %) compared to the springs of 2015, 2016, 2017 and 2019, respectively. In contrast, a small reduction of -3.4 ± 136 g C m^{-2} (-0.45 %) was observed for 2020 compared to 2018.

3.2. GPP anomalies by plant functional type

The positive GPP anomaly was observed in all ecosystems with short vegetation (grassland, savannah and shrubland) and eight out of 11 deciduous broadleaf (DBFs) or mixed forests (MFs). On the other hand, the majority of evergreen needleleaf forests (ENFs) (9/12 sites) and three DBFs exhibited a negative GPP anomaly. Meanwhile, the sites with no significant change in GPP, ranging from -7 % to $+4.1$ %, included all four wetlands (WETs), three ENFs, one grassland site (GRA), one mixed forest (MF) and one open shrubland site (OSH) (Table S1, Fig. S3).

The midday Bowen ratio (β), a ratio of sensible heat flux to latent heat flux, which is directly influenced by stomatal conductance in a given canopy, remained almost unchanged in GRA, SAV and OSH sites, and was < 1.0 in 2020. In forests (DBF, EBF, ENF and MF), there was a stronger negative relationship between the anomalies in GPP and β (Fig. 4), suggesting that the spring 2020 GPP in these ecosystems might have been impacted by atmospheric or soil dryness.
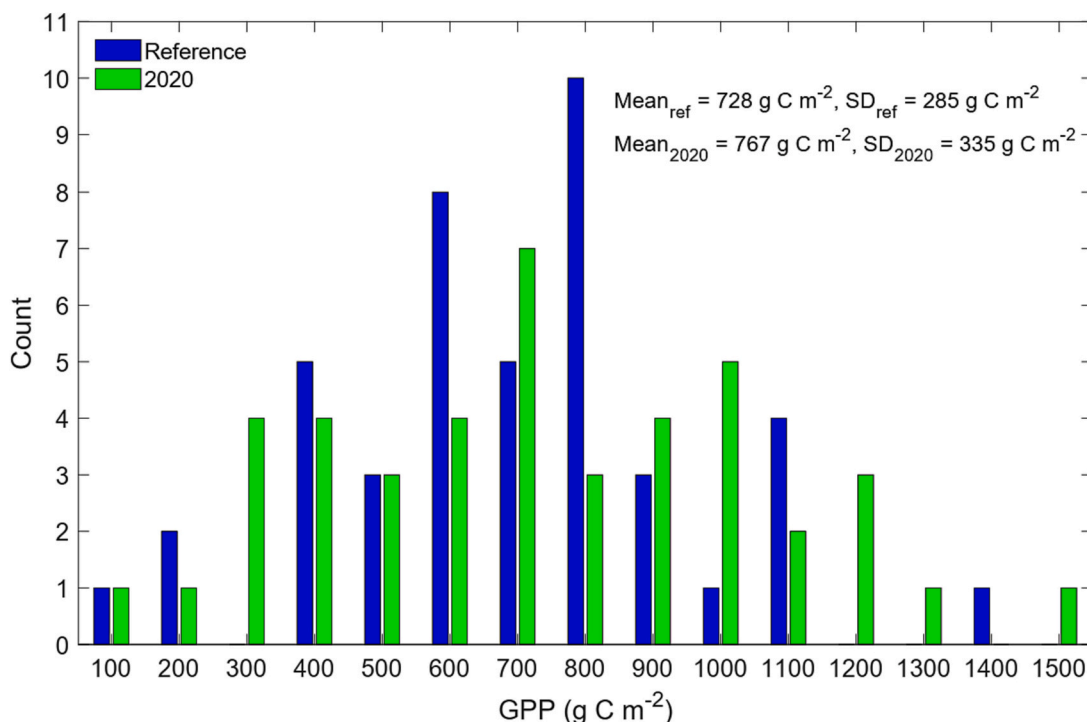
Fig. 2. Comparison of frequency distribution of gross primary production (GPP) across study sites in Europe between the springs of reference years (blue bars) and 2020 (green bars).
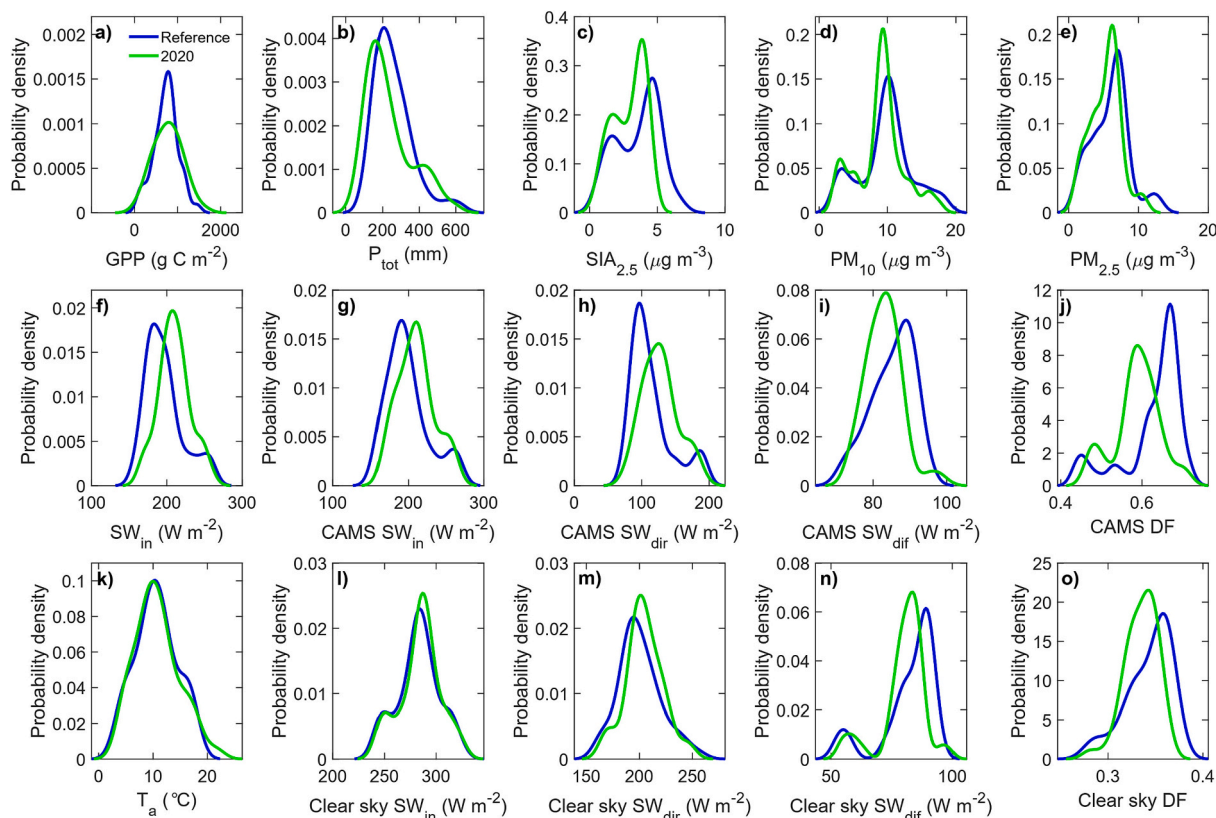
Fig. 3. Comparison of reference (blue line) and 2020 spring (green line) probability density distribution across 44 sites in Europe for (a) GPP (gross primary production), (b) P_{tot} (precipitation), (c) $SIA_{2.5}$ (secondary inorganic aerosol smaller than 2.5 μm), (d) PM_{10} (particulate matter smaller than 10 μm), (e) $PM_{2.5}$ (particulate matter smaller than 2.5 μm), (f) SW_{in}, (incoming shortwave radiation, measured on-site), (g) SW_{in} from the Copernicus Atmosphere Monitoring Service (CAMS), (h) CAMS SW_{dir} (direct radiation), (i) CAMS SW_{dif} (diffuse radiation), (j) CAMS DF (diffuse fraction), (k) T_a (air temperature), (l) clear sky SW_{in}, (m) clear sky SW_{dir}, (n) clear sky SW_{dif} and (o) clear sky DF.

| Year compared	ΔGPP (g C m^{-2})	ΔSW$_{in}$ (W m^{-2})	ΔT$_a$ (°C)
2015	+44 ± 178	+15 ± 17	+0.54 ± 1.0
2016	+35 ± 144	+24 ± 18	+0.58 ± 0.88
2017	+62 ± 129	+9.0 ± 17	−0.21 ± 1.3
2018	−3.4 ± 136	+12 ± 12	−0.30 ± 0.98
2019	+43 ± 137	+7.7 ± 16	−0.02 ± 1.2

3.3. Attributions of GPP anomalies

To investigate potential mechanisms underlying the GPP anomalies across the 34 sites where the GPP change was significant, we compared the 2020 GPP derived from eddy covariance measurements with the GPP simulated by empirical/semi-empirical models, which were constructed using meteorological and pollutant variables over the reference period for each site (Fig. 5). We categorised these 34 sites into three groups based on the contribution of meteorological and pollutant variables to the models, and the occurrence of management operations (Fig. 6, Table S4).

3.3.1. GPP anomalies explained by meteorology

Group 1 consists of 24 sites where the meteorology-based model explained > 53 % of the variance in GPP, with the exceptions of CH-Aws, CH-Dav, DE-Hai and DE-Hzd (see discussion in Sections 4.1 and 4.4). The contribution of pollutant variables to the total variance was < 6 % (Table S4). These sites, at which no agricultural or forest management occurred in spring 2020, experienced brighter, warmer and drier conditions compared to the reference years of 2015–2019. Specifically, there was an increase in mean SW$_{in}$ by +15 ± 11 W m^{-2}, T$_a$ by +0.2 ± 1.2 °C, and VPD by +0.06 ± 0.07 kPa. Conversely, P$_{tot}$ and soil water content (SWC) decreased by −36 ± 82 mm and −0.04 ± 0.06 m^{3}m^{-3},

respectively. Among these sites, 11 out of 24 sites experienced a reduction in GPP (−105 ± 63 g C m^{-2}, −14 %), while the remaining 13 sites showed an increase in GPP (+134 ± 94 g C m^{-2}, +17 %).

- **Impact of atmospheric and soil water limitations.** The reduction in GPP observed in 10 sites coincided with an increased Bowen ratio, β (+0.55 ± 0.44, +32 %, p < .001), indicating tighter stomatal control in spring 2020. This anomaly was accompanied by higher VPD (+0.03 ± 0.04 kPa, +8.2 %, p = .02) and lower SWC (−0.06 ± 0.06 m^3 m^{-3}, −23 %, p = .005). Furthermore, at these sites, the mean canopy radiation-use efficiency (α) and the maximal rate of photosynthesis (P$_{max}$) decreased by −0.01 ± 0.02 μmol CO$_2$ J^{-1} (−11 %, p = .13) and −3.7 ± 3.6 μmol CO$_2$ m^{-2} s^{-1} (−20 %, p = .006), respectively. Interestingly, the decline in GPP was concurrent with a continuous reduction in SWC at five forests (CH-Dav, DE-Hai, DE-Hzd, DE-Obe and DE-Tha) from summer 2018 to spring 2020, reaching their minimum values (Fig. S4). In addition to P$_{tot}$ deficits (−45 ± 65 mm, −19 %, p = .20), ET also declined by −44 ± 45 mm (−24 %, p = .09). Apart from drought effects, the decline in GPP at the boreal spruce forest (RU-Fy2) might be attributed to other factors. The relative change in β was +5.9 %, lower than other sites with Δβ > +10 %, and SW$_{in}$ decreased by −5.9 W m^{-2} (−3.3 %, p = .37) in relation to higher P$_{tot}$ (+30 mm, +13 %, p = .57), suggesting limited drought impact at this site.

- **Impact of global solar radiation.** At the 13 sites from Group 1 which had a positive GPP anomaly, the average increase in β was not significant (+0.17 ± 0.45, +11 %, p = .19). A significant increase in SW$_{in}$ was observed at 12 out of 13 sites (+19 ± 12 W m^{-2}, +9.8 %, p < .001), except for an alpine grassland, CH-Aws (1978 m a.s.l.). This coincides with reduced P$_{tot}$ (−26 ± 85 mm, −9.7 %, p = .3), SIA$_{2.5}$ (−0.87 ± 0.62 μg m^{-3}, −21 %, p < .001), PM$_{2.5}$ (−0.96 ± 0.67 μg m^{-3}, −14 %, p < .001) and PM$_{10}$ (−1.0 ± 0.7 μg m^{-3}, −9 %, p < .001). Further, α and P$_{max}$ increased by +0.02 ± 0.02 μmol CO$_2$ J^{-1} (+18 %, p = .04) and + 2.5 ± 10 μmol CO$_2$ m^{-2} s^{-1} (+9.3 %, p = .4) on average at these sites, respectively.
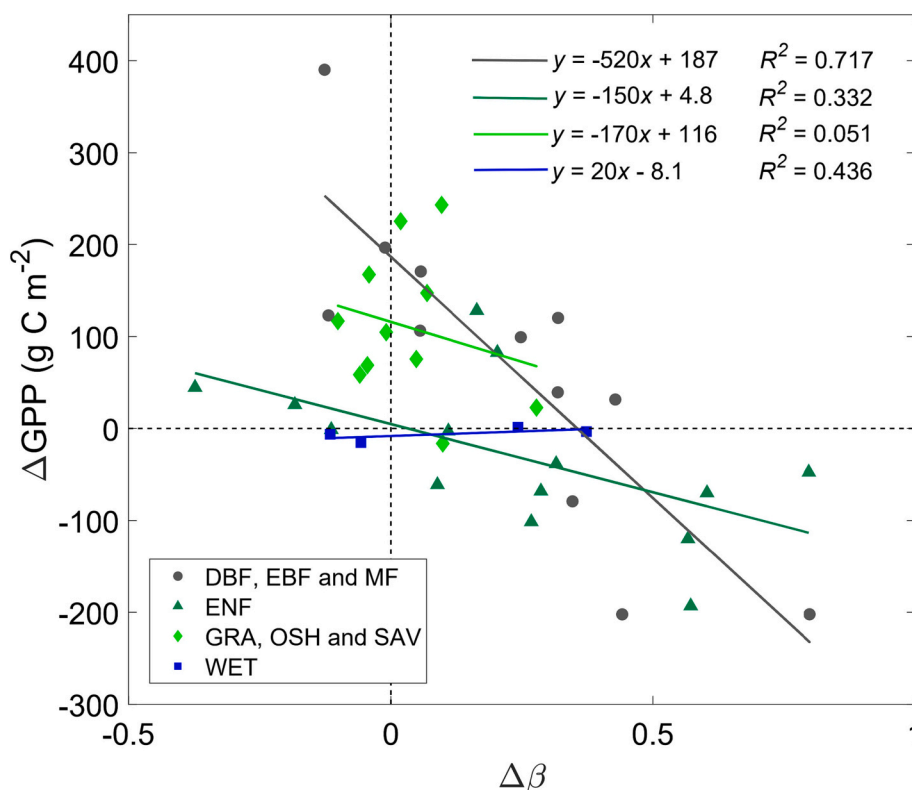
Fig. 4. Relationship between anomalies in gross primary production (ΔGPP) and anomalies in Bowen ratio (Δβ) across study sites from four classes of plant functional types (PFTs) during the spring of 2020, compared with the reference period. Solid lines represent linear regression lines of each PFT class. Abbreviations for PFTs: DBF, deciduous broadleaf forest; EBF, evergreen broadleaf forest; ENF, evergreen needleleaf forest; GRA, grassland; MF, mixed forest; OSH, open shrubland; SAV, savannah; WET, wetland.
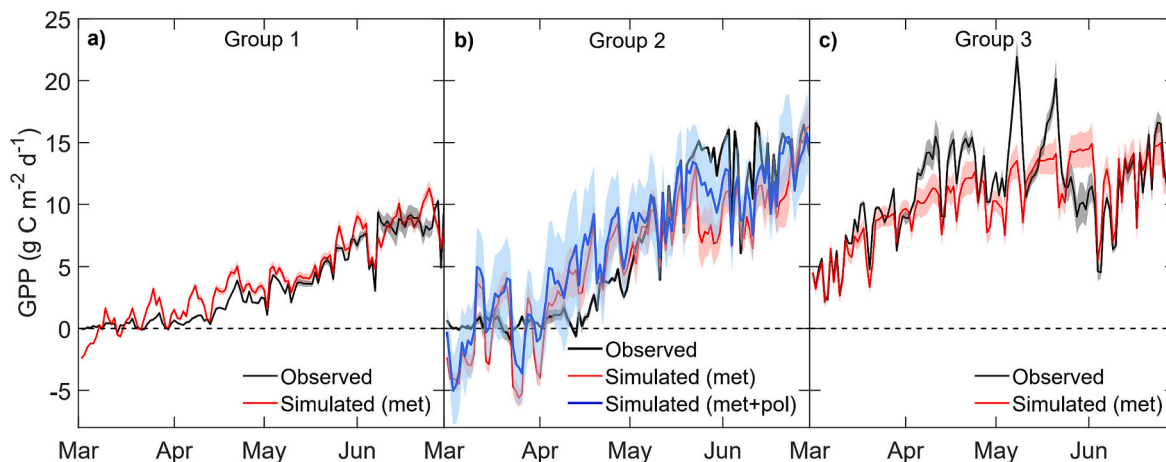
Fig. 5. Classification of study sites into three groups based on model simulations. Comparison of daily GPP values between observation-based estimates (black line) and meteorology-based models (red line, a-c), and meteorology+pollution-based models (blue line, b) from March to June 2020. The simulation patterns of each group representative are shown: (a) SE-Svb (ENF) for Group 1, (b) IT-MBo (GRA) for Group 2 and (c) BE-Dor (GRA) for Group 3. All meteorological and pollutant variables were included in the model simulations for all study sites in the three groups. However, only Group 2 exhibited a significant improvement in model performance with the inclusion of pollutants, as indicated by the blue line. For Groups 1 and 3, the improvement in model performance with the inclusion of pollutants (not shown) was not significant. Peak divergences in the observed GPP in (c) are attributed to management practices. Grey shaded areas indicate observation based GPP uncertainty. Red and blue shaded areas represent the 95 % confidence intervals on model-predicted values.
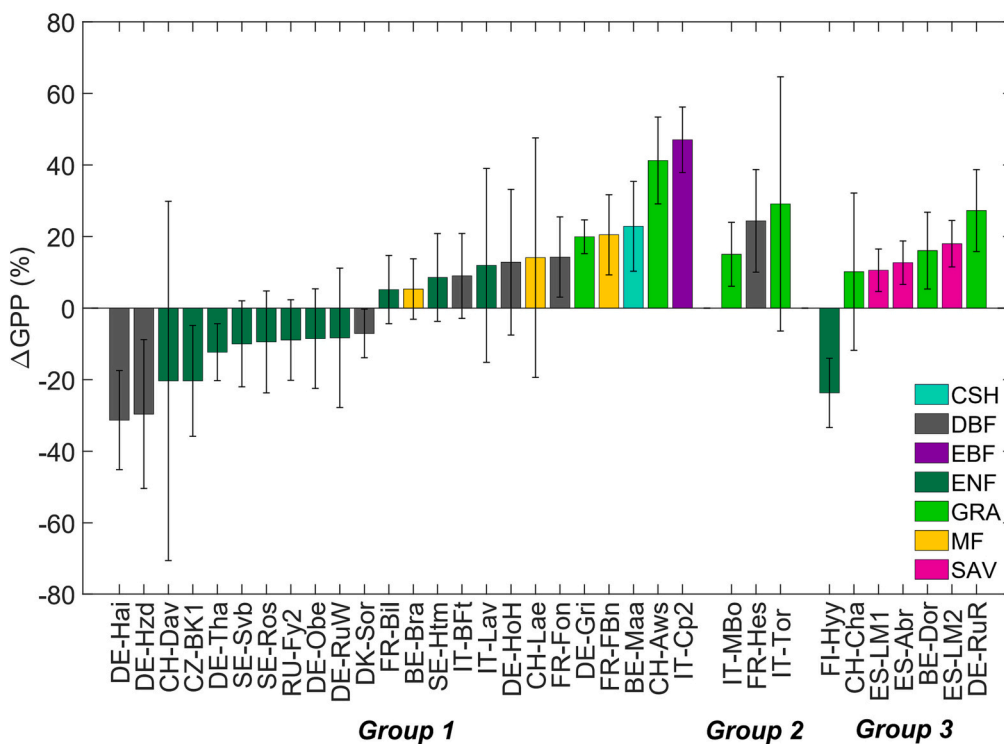
Fig. 6. The distribution of the relative change in gross primary production (GPP) in the spring of 2020 (March–June) relative to the spring average for 2015–2019 reference period at the three groups of study sites in Europe. Error bars represent one-sided uncertainty in the GPP anomaly.

3.3.2. GPP anomalies explained by meteorology and air pollution

Group 2 consists of two alpine grasslands, IT-MBo (1550 m a.s.l.) and IT-Tor (2160 m a.s.l.), along with a broadleaf forest, FR-Hes. These sites exhibited significant increases in GPP: IT-MBo ($+105 \pm 62$ g C m^{-2}, $+15$ %), IT-Tor ($+75 \pm 92$ g C m^{-2}, $+29$ %), and FR-Hes ($+197 \pm 116$ g C m^{-2}, $+24$ %). Across all sites, there was a substantial increase in α ($+0.05 \pm 0.03$ μmol CO_2 J^{-1}, $+71$ %, $p = .12$) and P_{max} ($+6.4 \pm 6.2$ μmol CO_2 m^{-2} s^{-1}, $+56$ %, $p = .13$). Given that IT-MBo is a meadow that is extensively managed with low mineral fertilisation and cut once a year in mid-July, IT-Tor is an unmanaged grassland, and FR-Hes

experienced no management-induced disturbance in 2020, it is evident that spring GPP anomaly in this group cannot be attributed to management practices. During both the reference period and the spring of 2020, IT-MBo showed concentrations of PM$_{2.5}$ and PM$_{10}$ that were more than twice as high as those at IT-Tor, despite similar relative changes. Additionally, FR-Hes consistently exhibited the highest concentrations of O_3, SO_2 and NH_3 throughout the study period. The analysis revealed that at FR-Hes, IT-MBo and IT-Tor, atmospheric pollutants contributed to 12 %, 8.7 % and 11 % of the variance in GPP, respectively, resulting in an improvement in NRMSE by 11 %, 8.3 % and 6 %. At FR-Hes and IT-

MBo, there was increase in SW_{in} ($+23 \pm 1.9$ W m^{-2}, $+11$ %, $p = .04$) and a decrease in SW_{dif} (-5 ± 1.2 W m^{-2}, -5.5 %, $p = .11$), which coincided with reductions in the concentrations of $SIA_{2.5}$ (-1.4 ± 0.98 μg m^{-3}, -29 %, $p = .10$), $PM_{2.5}$ (-1.5 ± 0.99 μg m^{-3}, -16 %, $p = .28$) and PM_{10} (-1.6 ± 1.0 μg m^{-3}, -13 %, $p = .27$). Notably, there was a decrease in P_{tot} by -82 mm (-25 %, $p < .01$) at FR-Hes and an increase in P_{tot} ($+83$ mm, $+20$ %, $p < .001$) at IT-MBo (Table S2). In the case of IT-Tor, mean SW_{in}, SW_{dif}, $SIA_{2.5}$, $PM_{2.5}$ and PM_{10} decreased by -2.6 W m^{-2} (-1.2 %, $p = .24$), -2.9 W m^{-2} (-3.5 %, $p = .001$), -0.97 μg m^{-3} (-20 %, $p < .001$), -1.4 μg m^{-3} (-29 %, $p < .001$) and -0.99 μg m^{-3} (-15 %, $p < .001$), respectively, in spring 2020, while P_{tot} increased by $+22$ mm ($+6.5$ %, $p = .41$) (Table S2 and S3).

3.3.3. GPP anomalies affected by management practices

Group 3 comprises one forest site, three productive grasslands (GRA) and three savannahs (SAV) that were subjected to various management practices including forest thinning (FI-Hyy), cutting and fertilizer application (BE-Dor, CH-Cha and DE-RuR), grazing (ES-Abr), or grazing and nutrient manipulation experiment (ES-LM1 and ES-LM2). Our analysis revealed that meteorological factors accounted for < 55 % of the variation in GPP at these sites. Thinning operations at FI-Hyy in January 2020 resulted in a 40 % reduction in LAI (Aslan et al., 2023; Mammarella et al., 2023), and a significant decline in spring GPP (-120 ± 49 g C m^{-2}, -24 %, $p < .001$). Conversely, the remaining sites of the group experienced an increase in GPP during 2020 ($+81 \pm 31$ g C m^{-2}, 14 %), with GRAs showing a greater increase ($+192 \pm 48$ g C m^{-2}, $+16$ %) compared to SAVs ($+81 \pm 31$ g C m^{-2}, $+14$ %). The difference in GPP can be partly attributed to positive anomalies in SW_{in} at GRAs ($+26 \pm 6.4$ W m^{-2}, $+14$ %, $p = .02$), accompanied by a decrease in SW_{dif} (-7.6 ± 2.0 W m^{-2}, -8.7 %, $p = .02$). In contrast, SAVs exhibited reduced SW_{in} (-11 ± 4.2 W m^{-2}, -4.5 %, $p = .04$) and increased SW_{dif} ($+6.4 \pm 0.76$ W m^{-2}, $+8.6$ %). The negative response of ΔT_a on ΔGPP in the SAVs, as opposed to the GRAs (Fig. S5) can be attributed to warmer temperature ($+0.46 \pm 0.08$ °C, $+2.7$ %, $p = .01$) and decreased water availability ($\Delta P_{tot} = -14 \pm 16$ mm, -8.1 %, $p = .27$), leading to early senescence in spring 2020.

4. Discussion

Using a 6-year time series from a network of 44 CO_2 flux monitoring sites, we successfully detected subtle year-to-year changes in spring GPP, and examined the underlying factors driving these changes. Our findings unveiled a significant GPP anomaly in 34 out of 44 European study sites, with 12 sites experiencing a negative anomaly and the remaining 22 sites showing a positive anomaly. This anomaly coincided with substantial changes in soil and atmospheric dryness, solar irradiance, air pollutants and vegetation management practices. Through our statistical approach, we were able to identify which group of variables – meteorology or pollutants – contributed most to the GPP anomaly. In the subsequent subsections, we discuss the extent to which these factors might have influenced the spring 2020 anomaly and explore potential connections – or lack thereof − with the impact of lockdown measures on atmospheric composition.

4.1. Drought-related reduction in GPP

Nearly all sites which experienced a GPP decrease in spring 2020 were affected by soil dryness (lower-than-usual SWC) or atmospheric drought (higher-than-usual VPD), as indicated by a significant positive anomaly in the Bowen ratio. A strong reduction in ET supports the hypothesis of stomatal closure in these ecosystems, mostly forests. However, the considerable decrease in the canopy radiation-use efficiency (α) suggests that biochemical (non-stomatal) processes also played a role in inhibiting photosynthesis in response to drought stress, in line with previous studies (Escalona et al., 1999; Gourlez de la Motte et al., 2020). Drought causes reductions in terrestrial ecosystem production (Ciais

et al., 2005; Zhao and Running, 2010) through stomatal closure and/or metabolic limitation (Flexas and Medrano, 2002), with effects on GPP that can be either immediate (e.g. stomatal closure) or delayed (e.g. altered hydraulic conductance, metabolic capacity, leaf longevity, or ecosystem composition) (Fu et al., 2022; Liu et al., 2019; Pereira et al., 2007; Yu et al., 2022). Indeed, Europe experienced one of the most severe droughts in the 21st century during the summer of 2018 and to a lesser extent 2019 (Bastos et al., 2020; Buras et al., 2020; Schuldt et al., 2020). The legacy effects of this drought on vegetation may have persisted until 2020 at CH-Dav, DE-Hai, DE-Hzd, DE-Obe and DE-Tha (Fig. 7). Trees are particularly susceptible to insect and pathogen outbreaks under prolonged or extreme drought (Jactel et al., 2012), which can lead to mortality and a shift in forest structure and composition (Li et al., 2021). These legacy effects which are not incorporated in the model may explain in part the relatively large discrepancies between observed and predicted GPP, especially at more severely drought-impacted sites such as CH-Dav, DE-Hai and DE-Hzd ($R^2 < 0.43$, NRMSE < 25 %). While other sites experienced a negative GPP anomaly due to drought, the afforested peatbog RU-Fy2 was the only site where this anomaly was not linked to dry conditions. Instead, excess rainfall may have created anaerobic conditions that weakened the photosynthetic activity of spruce trees.

### 4.2. Positive GPP anomalies were associated with an enhancement in solar irradiance

Our findings indicate that the positive GPP anomaly was primarily driven by enhanced SW_{in}, which outweighed the combined negative effects of increased VPD, reduced P_{tot} and DF. In spring 2020, we observed a main shift in the distribution of the diffuse fraction, from 0.67 to 0.59 for the peak value (Fig. 3j). This change is beyond the range where the increase in diffuse fraction has a fertilizing effect on GPP, which is typically below 0.45 (Knohl and Baldocchi, 2008; Ezhova et al., 2018; Park et al., 2018). Additionally, T_a remained relatively stable compared to previous springs, suggesting a limited contribution to the GPP anomaly.

There remains debate as to the extent to which the radiation anomalies should be attributed to changes in aerosol optical depth (i.e. COVID-19 induced changes in anthropogenic pollutant emissions) or changes in cloudiness. A recent study by Voigt et al. (2022) reported that the lower aerosol optical thickness during the lockdown led to increased SW_{in} over Europe. The clear sky irradiance anomalies observed in 2020 anomalies (Fig. 3m-o) suggest a decline in aerosol optical depth in spring 2020, but the impact of aerosol concentration on the diffuse fraction of incoming radiation was hardly distinguishable from changes in cloud fraction due to lower atmospheric humidity (Fig. 3b). A combined analysis of ground-based and satellite observations supports the hypothesis that the observed irradiance enhancement was largely due to changes in cloud fraction in Western Europe (van Heerwaarden et al., 2021). Ground observations indicated that cloudiness and aerosol optical depth were both exceptionally low in spring 2020 over Europe.

4.3. Impacts of atmospheric pollutants on GPP

In a typical year, ozone (O_3) concentration in spring is usually too low (< 50 ppb on average) to cause acute harm to plants (Fares et al., 2013), particularly for central-northern European ecosystems when the plants are still dormant. These observations do not support the hypothesis that a change in O_3 mediated the COVID-19 effect on GPP. Furthermore, the small decrease in O_3 concentrations (-1.8 %) simulated by LOTOS-EUROS in spring 2020 would have a negligible effect on carbon assimilation.

The increases in α and P_{max} in Group 2 (FR-Hes, IT-MBo and IT-Tor) suggest that the stronger plant uptake of CO_2 in 2020 at these sites might be linked to reductions in pollutant exposure or deposition through photosynthesis pathway and/or stomata (Coyne and Bingham, 1978;
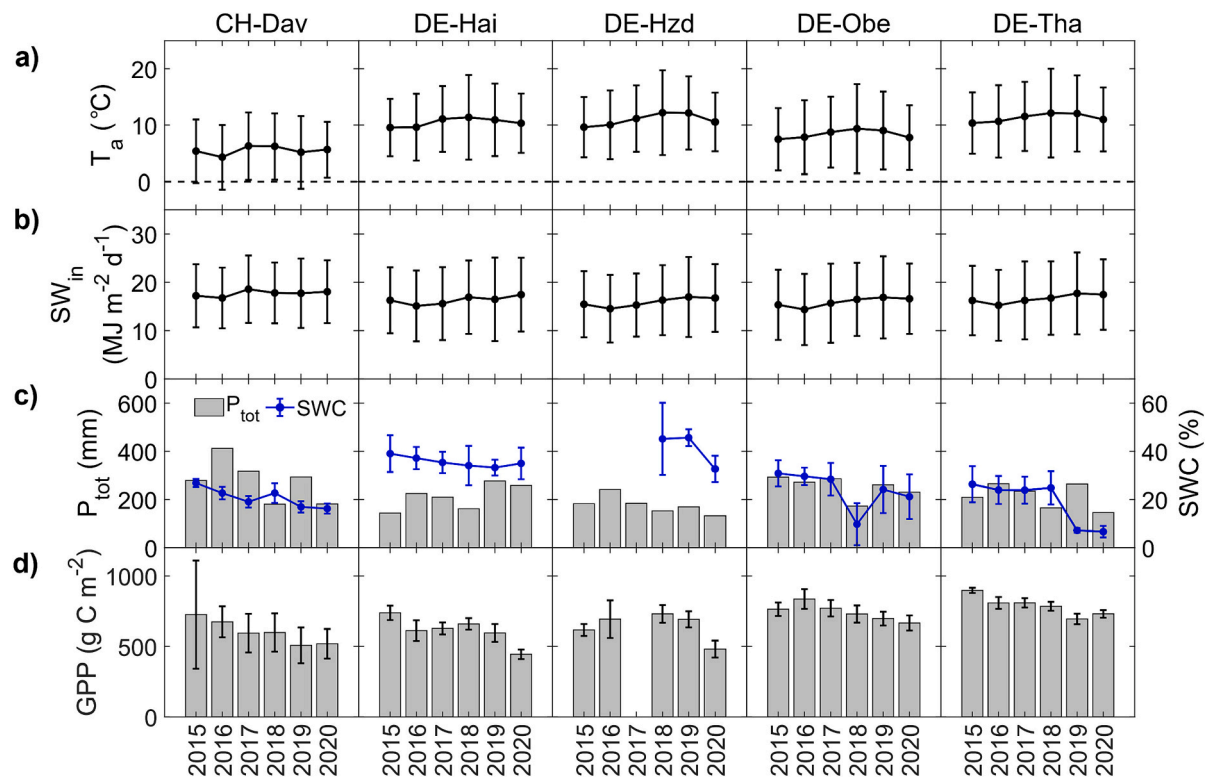
Fig. 7. Interannual variations of spring (averaged or summed from March to June) (a) air temperature (T_a), (b) incoming shortwave radiation (SW_{in}), (c) precipitation (P_{tot}) and soil water content (SWC), and (d) gross primary production (GPP) during the study period from 2015 to 2020 at two deciduous broadleaf forests (DE-Hai and DE-Hzd) and three evergreen needleleaf forests (CH-Dav, DE-Obe and DE-Tha) in Group 1. Each error bar for GPP denotes the one-sided uncertainty, while error bars for meteorological variables represent the standard deviation.

Philip, 2002). The long-range transboundary transport of air pollutants from the Po Valley has been demonstrated to affect not only the Italian Alpine region, but also other Italian regions and surrounding countries (Carbone et al., 2014; Diémoz et al., 2019a, 2019b; Finardi et al., 2014; Nyeki et al., 2002). With a population of over 20 million inhabitants, the Po Valley is one of the European pollution hotspots in northern Italy. Due to the valley's morphology and topography, pollutants are often trapped within the valley, which is enclosed by the Alps to the north and west, and the Apennine to the south. The aerosol particles, mainly of secondary origin from the Po Valley, can form layers that are advected by thermally driven winds or synoptic flows and extend up to 4000 m a. s.l. on the north-western Alps, potentially impacting high-altitude ecosystems through dry and wet deposition (Diémoz et al., 2019a, 2019b; Oldani et al., 2017; Wang et al., 2023). However, aerosol deposition occurs mainly on non-stomatal leaf surfaces and the ground, rather than diffusing through stomata like gases. Overall, the potential impact of aerosols on ecosystem functioning may be mediated through soil processes, stomatal transpiration, or migration of solutes on the leaf surface (Burkhardt, 2010; Burkhardt et al., 2012). While the direct link between aerosol deposition and phytotoxicity is not well-established, further research is needed to investigate these relationships. Similarly, previous studies have shown that NH_3 and $PM_{2.5}$ originating from the northeast of France (Bressi et al., 2014; Sciare et al., 2010; Viatte et al., 2021), where FR-Hes is located, have a significant impact due to long-range transport over Paris. Our findings are consistent with these studies, as FR-Hes is exposed to agricultural fields in the prevailing wind direction and ranked among the top four or six forest sites with the highest relative reduction in concentrations of $PM_{2.5}$, PM_{10} and SO_2, as well as a relative increase in NH_3 concentration.

4.4. Limitations and confounding effects: Timing of snow melt, lagged effects and management practices

One limitation of our approach is that the model simulation cannot account for all known drivers of GPP and ecosystem behaviour that occurred during the reference period. This can result in the underestimation or overestimation of GPP. For example, the timing of snow melt at continental locations or upland sites, which is not considered in the models, likely contributes to the divergence observed over nearly the entire duration of spring 2020 for CH-Aws and IT-Tor ($R^2 < 0.53$, NRMSE < 32 %). Snow cover is a critical factor that affects the phenology and productivity of high-altitude vegetation in the European Alps (Choler, 2015; Xie et al., 2017). The anomalously warm winter 2019–2020 at these sites (T_a: $+1.7 \pm 0.39$ °C, $+58$ %, $p < .001$) resulted in less snowfall and earlier spring melts (Barnett et al., 2005), thus advancing the onset of the growing season and extending the carbon uptake period in spring (Desai et al., 2016).

On the other hand, the warm winter experienced in Europe during 2019–2020, as reported by the Copernicus Climate Change Service (2021) had a strong impact on the GPP during the following spring at two Mediterranean sites (FR-FBn and IT-Cp2) (Fig. S6). This extended warming effect made it difficult to use the reference spring data to accurately predict the 2020 spring GPP, resulting in a large divergence between the observed and simulated GPP (Fig. S7a-b). GPP models showed poor fit for these two sites, with negative values of R^2 and NRMSE (Table S4). We observed a significant improvement in the accuracy of our GPP models for both sites after using preceding winter and/or year-round data from January 2015 to February 2020 as input ($R^2 > 0.76$, NRMSE > 51 %) (Table S4, Fig. S7c-d). By using a relevant or larger dataset that includes more historical information, our models were better able to account for this anomalous warming effect and provide more accurate predictions of GPP. These findings highlight the

importance of incorporating relevant and comprehensive data when modelling ecosystem processes.

The Group 3 sites (FI-Hyy, BE-Dor, CH-Cha, DE-RuR, ES-Abr, ES-LM1 and ES-EM2) were subjected to a range of management practices such as thinning, cutting, fertilizer application, grazing and nutrient manipulation experiment (El-Madany et al., 2021; Gharun et al., 2020), which confounded the patterns of GPP. For instance, intensive thinning resulted in a substantial decrease in LAI, and consequently reduced light interception by the canopy at FI-Hyy (Aslan et al., 2023; Mammarella et al., 2023). As a result, our data driven models were unable to fully capture the observed dynamics of GPP during spring 2020 at these sites (e.g. Fig. 5c) ($R^2 < 0.55$, NRMSE < 33 %). The inclusion of pollutant variables slightly improved the variability of GPP ($\Delta R^2 < 0.1$) and reduced the prediction error (ΔNRMSE < 4 %) across all sites, except for ES-LM1 and ES-LM2. These two sites exhibited higher R^2 ($0.07 < \Delta R^2 < 0.11$) and NRMSE values (4.4 % $< \Delta$NRMSE < 6.1 %), potentially due to more extensive application of nitrogen and phosphorus fertilizers in the experiments.

5. Conclusion

Our analysis emphasizes the importance of incorporating the eco-physiological responses of vegetation to climate and management when interpreting the changes in ecosystem photosynthesis observed during the spring of 2020. We successfully validated our first hypothesis that a network of 44 sites, using a six-year time series of CO_2 exchange could detect the gross primary production (GPP) anomaly in spring 2020. The findings reveal that the enhanced downwelling shortwave radiation played a dominant role in the overall enhancement of GPP, but only in the absence of soil and atmospheric drought, which negatively affected GPP and outweighed the radiation enhancement effect. These findings also highlight the importance of considering wet and dry years in GPP dynamics, as water availability plays a critical role in ecosystem responses to varying climatic conditions. Incorporating this aspect in the model is vital for accurate assessments of GPP dynamics and informing sustainable management practices.

However, our hypothesis that a substantial reduction in ozone precursors (such as NO_x) emissions would (i) decrease ecosystem ozone exposure, and (ii) indirectly alleviate its negative impact on GPP was not supported. The temporary changes in atmospheric pollutant deposition had only a marginal effect on GPP. While the 2020 lockdown led to a significant reduction in emissions across Europe, including CO_2, across Europe for a few months, this effect was well detected by the urban sites in the monitoring network (Nicolini et al., 2022). However, its primary impact on terrestrial GPP appears to be linked to reduced aerosol loadings and their impact on the radiation regime.

These results highlight the need for concerted policies that address global climate change, land resource management and air quality concurrently. Understanding complex interactions between ecosystem responses, climate and pollutant factors is crucial for devising effective strategies to mitigate future impacts on ecosystem photosynthesis and carbon cycling. As part of the scientific community, we can contribute to this understanding and collectively work towards a sustainable environment.

CRediT authorship contribution statement

DL and ACIT developed the conceptual framework for the analysis. ACIT conducted all data analysis and wrote the initial version of the manuscript. DL contributed to the writing, revision and editing of the manuscript. CRF and PCS reviewed and edited the manuscript. The remaining authors reviewed the manuscript and contributed to the discussion based on their expertise and the data collected from their research sites.

Declaration of competing interest

The authors declare that they have no known competing financial interests or personal relationships that could have appeared to influence the work reported in this paper.

Data availability

Fluxes and meteorological data are available at the ICOS Carbon Portal from doi:10.18160/2G60-ZHAK; LOTOS-EUROS estimates of air pollution data can be accessed through the Copernicus Atmosphere Monitoring Service https://atmosphere.copernicus.eu/; CAMS radiation data was downloaded from https://www.soda-pro.com/web-services/radiation/cams-radiation-service.

Appendix A. Supplementary data

Supplementary data to this article can be found online at https://doi.org/10.1016/j.scitotenv.2023.166149.

References

Akaike, H., 1976. A new look at the statistical model identification. IEEE Trans. Automat. Contr. 19, 716–723.

Aslan, T., Kolari, P., Launiainen, S., Peltola, O., Back, J., Vesala, T., Aalto, J., Mammarella, I., 2023. Short-term effect of thinning of carbon dioxide and water vapour fluxes in a boreal pine forest. Manuscr. Prep.

Barnett, T.P., Adam, J.C., Lettenmaier, D.P., 2005. Potential impacts of a warming climate on water availability in snow-dominated regions. Nature 438, 303–309. https://doi.org/10.1038/nature04141.

Barré, J., Petetin, H., Colette, A., Guevara, M., Peuch, V.H., Rouil, L., Engelen, R., Inness, A., Flemming, J., Pérez García-Pando, C., Bowdalo, D., Meleux, F., Geels, C., Christensen, J.H., Gauss, M., Benedictow, A., Tsyro, S., Friese, E., Struzewska, J., Kaminski, J.W., Douros, J., Timmermans, R., Robertson, L., Adani, M., Jorba, O., Joly, M., Kouznetsov, R., 2021. Estimating lockdown-induced European NO_2 changes using satellite and surface observations and air quality models. Atmos. Chem. Phys. 21, 7373–7394. https://doi.org/10.5194/acp-21-7373-2021.

Bartoń, K., 2020. MuMIn: Multi-Model Inference. R package version 1 (43), 17.

Bastos, A., Ciais, P., Friedlingstein, P., Sitch, S., Pongratz, J., Fan, L., Wigneron, J.P., Weber, U., Reichstein, M., Fu, Z., Anthoni, P., Arneth, A., Haverd, V., Jain, A.K., Joetzjer, E., Knauer, J., Lienert, S., Loughran, T., McGuire, P.C., Tian, H., Viovy, N., Zaehle, S., 2020. Direct and seasonal legacy effects of the 2018 heat wave and drought on European ecosystem productivity. Sci. Adv. 6, 1–14. https://doi.org/10.1126/sciadv.aba2724.

Bauwens, M., Compernolle, S., Stavrakou, T., Müller, J.F., van Gent, J., Eskes, H., Levelt, P.F., van Der A, R., Veefkind, J.P., Vlietinck, J., Yu, H., Zehner, C., 2020. Impact of coronavirus outbreak on NO_2 pollution assessed using TROPOMI and OMI observations. Geophys. Res. Lett. 47, 1–9. https://doi.org/10.1029/2020GL087978.

Bressi, M., Sciare, J., Ghersi, V., Mihalopoulos, N., Petit, J.E., Nicolas, J.B., Moukhtar, S., Rosso, A., Féron, A., Bonnaire, N., Poulakis, E., Theodosi, C., 2014. Sources and geographical origins of fine aerosols in Paris (France). Atmos. Chem. Phys. 14, 8813–8839. https://doi.org/10.5194/acp-14-8813-2014.

Buras, A., Rammig, A.S., Zang, C., 2020. Quantifying impacts of the 2018 drought on European ecosystems in comparison to 2003. Biogeosciences 17, 1655–1672. https://doi.org/10.5194/bg-17-1655-2020.

Burkhardt, J., 2010. Hygroscopic particles on leaves: nutrients or desiccants? Ecol. Monogr. 80, 369–399. https://doi.org/10.1890/09-1988.1.

Burkhardt, J., Basi, S., Pariyar, S., Hunsche, M., 2012. Stomatal penetration by aqueous solutions – an update involving leaf surface particles. New Phytol. 196, 774–787. https://doi.org/10.1111/j.1469-8137.2012.04307.x.

Carbone, C., Decesari, S., Paglione, M., Giulianelli, L., Rinaldi, M., Marinoni, A., Cristofanelli, P., Didiodato, A., Bonasoni, P., Fuzzi, S., Facchini, M.C., 2014. 3-year chemical composition of free tropospheric PM1 at the Mt. Cimone GAW global station - South Europe - 2165m a.s.l. Atmos. Environ. 87, 218–227. https://doi.org/10.1016/j.atmosenv.2014.01.048.

Choler, P., 2015. Growth response of temperate mountain grasslands to inter-annual variations in snow cover duration. Biogeosciences 12, 3885–3897. https://doi.org/10.5194/bg-12-3885-2015.

Ciais, P., Reichstein, M., Viovy, N., Granier, A., Ogée, J., Allard, V., Aubinet, M., Buchmann, N., Bernhofer, C., Carrara, A., Chevallier, F., De Noblet, N., Friend, A.D., Friedlingstein, P., Grünwald, T., Heinesch, B., Keronen, P., Knohl, A., Krinner, G., Loustau, D., Manca, G., Matteucci, G., Miglietta, F., Ourcival, J.M., Papale, D., Pilegaard, K., Rambal, S., Seufert, G., Soussana, J.F., Sanz, M.J., Schulze, E.D., Vesala, T., Valentini, R., 2005. Europe-wide reduction in primary productivity caused by the heat and drought in 2003. Nature 437, 529–533. https://doi.org/10.1038/nature03972.

Copernicus, 2021. 2020 Warmest Year on Record for Europe; Globally, 2020 Ties with 2016 for Warmest Year Recorded. Copernicus Clim. Chang. Serv. URL. https://climate.copernicus.eu/copernicus-2020-warmest-year-record-europe-globally-2020-ties-2016-warmest-year-recorded.

Coyne, P.I., Bingham, G.E., 1978. Photosynthesis and stomatal light responses in snap beans exposed to hydrogen sulfide and ozone. J. Air Pollut. Control Assoc. 28, 1119–1123. https://doi.org/10.1080/00022470.1978.10470715.

Desai, A.R., Wohlfahrt, G., Zeeman, M.J., Katata, G., Eugster, W., Montagnani, L., Gianelle, D., Mauder, M., Schmid, H.P., 2016. Montane ecosystem productivity responds more to global circulation patterns than climatic trends. Environ. Res. Lett. 11 https://doi.org/10.1088/1748-9326/11/2/024013.

Diémoz, H., Barnaba, F., Magri, T., Pession, G., Dionisi, D., Pittavino, S., Tombolato, I.K.F., Campanelli, M., Ceca, L.S. Della, Hervo, M., Di Liberto, L., Ferrero, L., Gobbi, G.P., 2019a. Transport of Po Valley aerosol pollution to the northwestern Alps – Part 1: Phenomenology. Atmos. Chem. Phys. 19, 3065–3095. https://doi.org/10.5194/acp-19-3065-2019.

Diémoz, H., Gobbi, G.P., Magri, T., Pession, G., Pittavino, S., Tombolato, I.K.F., Campanelli, M., Barnaba, F., 2019b. Transport of Po Valley aerosol pollution to the northwestern Alps – Part 2: Long-term impact on air quality. Atmos. Chem. Phys. 19, 10129–10160. https://doi.org/10.5194/acp-19-3065-2019.

El-Madany, T.S., Reichstein, M., Carrara, A., Martín, M.P., Moreno, G., Gonzalez-Cascon, R., Peñuelas, J., Ellsworth, D.S., Burchard-Levine, V., Hammer, T.W., Knauer, J., Kolle, O., Luo, Y., Pacheco-Labrador, J., Nelson, J.A., Perez-Priego, O., Rolo, V., Wutzler, T., Migliavacca, M., 2021. How nitrogen and phosphorus availability change water use efficiency in a Mediterranean savanna ecosystem. J. Geophys. Res. Biogeosci. 126 https://doi.org/10.1029/2020JG006005.

Escalona, J.M., Flexas, J., Medrano, H., 1999. Stomatal and non-stomatal limitations of photosynthesis under water stress in field-grown grapevines. Aust. J. Plant Physiol. 26, 421–433.

Ezhova, E., Ylivinkka, I., Kuusk, J., Komsaare, K., Vana, M., Krasnova, A., Noe, S., Arshinov, M., Belan, B., Park, S.Bin, Lavric, J.V., Heimann, M., Petäjä, T., Vesala, T., Mammarella, I., Kolari, P., Bäck, J., Rannik, U., Kerminen, V.M., Kulmala, M., 2018. Direct effect of aerosols on solar radiation and gross primary production in boreal and hemiboreal forests. Atmos. Chem. Phys. 18, 17863–17881. https://doi.org/10.5194/acp-18-17863-2018.

Falge, E., Baldocchi, D., Olson, R., Anthoni, P., Aubinet, M., Bernhofer, C., Burba, G., Ceulemans, R., Clement, R., Dolman, H., Granier, A., Gross, P., Grünwald, T., Hollinger, D., Jensen, N.O., Katul, G., Keronen, P., Kowalski, A., Lai, C.T., Law, B.E., Meyers, T., Moncrieff, J., Moors, E., Munger, J.W., Pilegaard, K., Rannik, Ü., Rebmann, C., Suyker, A., Tenhunen, J., Tu, K., Verma, S., Vesala, T., Wilson, K., Wofsy, S., 2001. Gap filling strategies for defensible annual sums of net ecosystem exchange. Agric. For. Meteorol. 107, 43–69. https://doi.org/10.1016/S0168-1923(00)00225-2.

Fares, S., Vargas, R., Detto, M., Goldstein, A.H., Karlik, J., Paoletti, E., Vitale, M., 2013. Tropospheric ozone reduces carbon assimilation in trees: estimates from analysis of continuous flux measurements. Glob. Chang. Biol. 19, 2427–2443. https://doi.org/10.1111/gcb.12222.

Finardi, S., Silibello, C., D'Allura, A., Radice, P., 2014. Analysis of pollutants exchange between the Po Valley and the surrounding European region. Urban Clim. 10, 682–702. https://doi.org/10.1016/j.uclim.2014.02.002.

Flechard, C.R., Ibrom, A., Skiba, U.M., De Vries, W., Van Oijen, M., Cameron, D.R., Dise, N.B., Korhonen, J.F.J., Buchmann, N., Legout, A., Simpson, D., Sanz, M.J., Aubinet, M., Loustau, D., Montagnani, L., Neirynck, J., Janssens, I.A., Pihlatie, M., Kiese, R., Siemens, J., Francez, A.J., Augustin, J., Varlagin, A., Olejnik, J., Juszczak, R., Aurela, M., Berveiller, D., Chojnicki, B.H., Dämmgen, U., Delpierre, N., Djuricic, V., Drewer, J., Dufrêne, E., Eugster, W., Fauvel, Y., Fowler, D., Frumau, A., Granier, A., Gross, P., Hamon, Y., Helfter, C., Hensen, A., Horvath, L., Kitzler, B., Kruijt, B., Kutsch, W.L., Lobo-Do-Vale, R., Lohila, A., Longdoz, B., Marek, M.V., Matteucci, G., Mitosinkova, M., Moreaux, V., Neftel, A., Ourcival, J.M., Pilegaard, K., Pita, G., Sanz, F., Schjoerring, J.K., Sebastià, M.T., Sim Tang, Y., Uggerud, H., Urbaniak, M., Van DIjk, N., Vesala, T., Vidic, S., Vincke, C., Weidinger, T., Zechmeister-Boltenstern, S., Butterbach-Bahl, K., Nemitz, E., Sutton, M.A., 2020a. Carbon–nitrogen interactions in European forests and semi-natural vegetation – Part 1: Fluxes and budgets of carbon, nitrogen and greenhouse gases from ecosystem monitoring and modelling. Biogeosciences 17, 1583–1620. https://doi.org/10.5194/bg-17-1583-2020.

Flechard, C.R., Van Oijen, M., Cameron, D.R., De Vries, W., Ibrom, A., Buchmann, N., Dise, N.B., Janssens, I.A., Neirynck, J., Montagnani, L., Varlagin, A., Loustau, D., Legout, A., Ziemblińska, K., Aubinet, M., Aurela, M., Chojnicki, B.H., Drewer, J., Eugster, W., Francez, A.J., Juszczak, R., Kitzler, B., Kutsch, W.L., Lohila, A.,

Longdoz, B., Matteucci, G., Moreaux, V., Neftel, A., Olejnik, J., Sanz, M.J., Siemens, J., Vesala, T., Vincke, C., Nemitz, E., Zechmeister-Boltenstern, S., Butterbach-Bahl, K., Skiba, U.M., Sutton, M.A., 2020b. Carbon–nitrogen interactions in European forests and semi-natural vegetation – Part 2: Untangling climatic, edaphic, management and nitrogen deposition effects on carbon sequestration potentials. Biogeosciences 17, 1621–1654. https://doi.org/10.5194/bg-17-1621-2020.

Flexas, J., Medrano, H., 2002. Drought-inhibition of photosynthesis in C3 plants: Stomatal and non-stomatal limitations revisited. Ann. Bot. 89, 183–189. https://doi.org/10.1093/aob/mcf027.

Fu, Z., Ciais, P., Prentice, I.C., Gentine, P., Makowski, D., Bastos, A., Luo, X., Green, J.K., Stoy, P.C., Yang, H., Hajima, T., 2022. Atmospheric dryness reduces photosynthesis along a large range of soil water deficits. Nat. Commun. 13, 1–10. https://doi.org/10.1038/s41467-022-28652-7.

Gharun, M., Hörtnagl, L., Paul-Limoges, E., Ghiasi, S., Feigenwinter, I., Burri, S., Marquardt, K., Etzold, S., Zweifel, R., Eugster, W., Buchmann, N., 2020. Physiological response of Swiss ecosystems to 2018 drought across plant types and elevation. Philos. Trans. R. Soc. B Biol. Sci. 375 https://doi.org/10.1098/rstb.2019.0521.

Gourlez de la Motte, L., Beauclaire, Q., Heinesch, B., Cuntz, M., Foltýnová, L., Šigut, L., Kowalska, N., Manca, G., Ballarin, I.G., Vincke, C., Roland, M., Ibrom, A., Lousteau, D., Siebicke, L., Neiryink, J., Longdoz, B., 2020. Non-stomatal processes reduce gross primary productivity in temperate forest ecosystems during severe edaphic drought: edaphic drought in forest ecosystems. Philos. Trans. R. Soc. B Biol. Sci. 375 https://doi.org/10.1098/rstb.2019.0527.

Grene, R., 2002. Oxidative stress and acclimation mechanisms in plants. Arab. B. 1, e0036 https://doi.org/10.1199/tab. 0036.1.

Gschwind, B., Wald, L., Blanc, P., Lefèvre, M., Schroedter-Homscheidt, M., Arola, A., 2019. Improving the McClear model estimating the downwelling solar radiation at ground level in cloud-free conditions - McClear-v3. Meteorol. Zeitschrift 28, 147–163. https://doi.org/10.1127/metz/2019/0946.

Guevara, M., Jorba, O., Soret, A., Petetin, H., Bowdalo, D., Serradell, K., Tena, C., Van Der Gon, H.D., Kuenen, J., Peuch, V.H., Pérez Garciá-Pando, C., 2021. Time-resolved emission reductions for atmospheric chemistry modelling in Europe during the COVID-19 lockdowns. Atmos. Chem. Phys. 21, 773–797. https://doi.org/10.5194/acp-21-773-2021.

van Heerwaarden, C.C., Mol, W.B., Veerman, M.A., Benedict, I., Heusinkveld, B.G., Knap, W.H., Kazadzis, S., Kouremeti, N., Fiedler, S., 2021. Record high solar irradiance in Western Europe during first COVID-19 lockdown largely due to unusual weather. Commun. Earth Environ. 2, 1–7. https://doi.org/10.1038/s43247-021-00110-0.

Hollinger, D.Y., Richardson, A.D., 2005. Uncertainty in eddy covariance measurements and its application to physiological models. Tree Physiol. 25, 873–885. https://doi.org/10.1093/treephys/25.7.873.

Jactel, H., Petit, J., Desprez-Loustau, M.L., Delzon, S., Piou, D., Battisti, A., Koricheva, J., 2012. Drought effects on damage by forest insects and pathogens: a meta-analysis. Glob. Chang. Biol. 18, 267–276. https://doi.org/10.1111/j.1365-2486.2011.02512.x.

Knohl, A., Baldocchi, D.D., 2008. Effects of diffuse radiation on canopy gas exchange processes in a forest ecosystem. J. Geophys. Res. Biogeosciences 113, 1–17. https://doi.org/10.1029/2007JG000663.

Lasslop, G., Reichstein, M., Papale, D., Richardson, A., Arneth, A., Barr, A., Stoy, P., Wohlfahrt, G., 2010. Separation of net ecosystem exchange into assimilation and respiration using a light response curve approach: critical issues and global evaluation. Glob. Chang. Biol. 16, 187–208. https://doi.org/10.1111/j.1365-2486.2009.02041.x.

Lefèvre, M., Oumbe, A., Blanc, P., Espinar, B., Gschwind, B., Qu, Z., Wald, L., Schroedter-Homscheidt, M., Hoyer-Klick, C., Arola, A., Benedetti, A., Kaiser, J.W., Morcrette, J.J., 2013. McClear: a new model estimating downwelling solar radiation at ground level in clear-sky conditions. Atmos. Meas. Tech. 6, 2403–2418. https://doi.org/10.5194/amt-6-2403-2013.

Li, X., Wang, Y.P., Lu, X., Yan, J., 2021. Diagnosing the impacts of climate extremes on the interannual variations of carbon fluxes of a subtropical evergreen mixed forest. Agric. For. Meteorol. 307, 108507 https://doi.org/10.1016/j.agrformet.2021.108507.

Liu, P., Zha, T., Jia, X., Black, T.A., Jassal, R.S., Ma, J., Bai, Y., Wu, Y., 2019. Different effects of spring and summer droughts on ecosystem carbon and water exchanges in a semiarid Shrubland ecosystem in Northwest China. Ecosystems 22, 1869–1885. https://doi.org/10.1007/s10021-019-00379-5.

Mammarella, I., Thomas, A., Aslan, T., Aalto, J., Back, J., Kolari, P., Launiainen, S., Peltola, O., Vesala, T., 2023. Effect of thinning on turbulence structure, energy and gas exchange in a boreal forest. In: EGU general assembly 2023. https://doi.org/10.5194/egusphere-egu23-12230. Vienna.

Manders, A.M.M., Builtjes, P.J.H., Curier, L., Gon, H.A.C.D. Vander, Hendriks, C., Jonkers, S., Kranenburg, R., Kuenen, J.J.P., Segers, A.J., Timmermans, R.M.A., Visschedijk, A.J.H., Kruit, R.J.W., Pul, W.A.J.V., Sauter, F.J., Van Der Swaluw, E., Swart, D.P.J., Douros, J., Eskes, H., Van Meijgaard, E., Van Ulft, B., Van Velthoven, P., Banzhaf, S., Mues, A.C., Stern, R., Fu, G., Lu, S., Heemink, A., Van Velzen, N., Schaap, M., 2017. Curriculum vitae of the LOTOS-EUROS (v2.0) chemistry transport model. Geosci. Model Dev. 10, 4145–4173. https://doi.org/10.5194/gmd-10-4145-2017.

Manders-Groot, A.M.M., Segers, A.J., Jonkers, S., Schaap, M., Timmermans, R., Hendriks, C., Sauter, F., Kruit, R.W., Swaluw, E. Van Der, Eskes, H., Banzhaf, S., 2016. LOTOS-EUROS v2.0 Reference Guide. TNO Rep. 2016 R10898 77.

MathWorks, 2022. MATLAB function: compare. https://www.mathworks.com/help/ident/ref/compare.html.

Menut, L., Bessagnet, B., Siour, G., Mailler, S., Pennel, R., Cholakian, A., 2020. Impact of lockdown measures to combat Covid-19 on air quality over western Europe. Sci. Total Environ. 741, 140426 https://doi.org/10.1016/j.scitotenv.2020.140426.

Mercado, L.M., Bellouin, N., Sitch, S., Boucher, O., Huntingford, C., Wild, M., Cox, P.M., 2009. Impact of changes in diffuse radiation on the global land carbon sink. Nature 458, 1014–1017. https://doi.org/10.1038/nature07949.

Nicolini, G., Antoniella, G., Carotenuto, F., Christen, A., Ciais, P., Feigenwinter, C., Gioli, B., Stagakis, S., Velasco, E., Vogt, R., Ward, H.C., Barlow, J., Chrysoulakis, N., Duce, P., Graus, M., Helfter, C., Heusinkveld, B., Järvi, L., Karl, T., Marras, S., Masson, V., Matthews, B., Meier, F., Nemitz, E., Sabbatini, S., Scherer, D., Schume, H., Sirca, C., Steeneveld, G.J., Vagnoli, C., Wang, Y., Zaldei, A., Zheng, B., Papale, D., 2022. Direct observations of CO$_2$ emission reductions due to COVID-19 lockdown across European urban districts. Sci. Total Environ. 830 https://doi.org/10.1016/j.scitotenv.2022.154662.

Nyeki, S., Eleftheriadis, K., Baltensperger, U., Colbeck, I., Fiebig, M., Fix, A., Kiemle, C., Lazaridis, M., Petzold, A., 2002. Airborne lidar and in-situ aerosol observations of an elevated layer, leeward of the european alps and apennines. Geophys. Res. Lett. 29, 3–6. https://doi.org/10.1029/2002GL014897.

Oldani, K.M., Mladenov, N., Williams, M.W., Campbell, C.M., Lipson, D.A., 2017. Seasonal patterns of dry deposition at a high-elevation site in the Colorado Rocky Mountains. J. Geophys. Res. Atmos. 122, 11183–11200.

Ordóñez, C., Garrido-Perez, J.M., García-Herrera, R., 2020. Early spring near-surface ozone in Europe during the COVID-19 shutdown: Meteorological effects outweigh emission changes. Sci. Total Environ. 747, 141322 https://doi.org/10.1016/j.scitotenv.2020.141322.

Park, S.Bin, Knohl, A., Lucas-Moffat, A.M., Migliavacca, M., Gerbig, C., Vesala, T., Peltola, O., Mammarella, I., Kolle, O., Lavric, J.V., Prokushkin, A., Heimann, M., 2018. Strong radiative effect induced by clouds and smoke on forest net ecosystem productivity in central Siberia. Agric. For. Meteorol. 250–251, 376–387. https://doi.org/10.1016/j.agrformet.2017.09.009.

Pastorello, G., Trotta, C., Canfora, E., Chu, H., Christianson, D., Cheah, Y.W., Poindexter, C., Chen, J., Elbashandy, A., Humphrey, M., Isaac, P., Polidori, D., Ribeca, A., van Ingen, C., Zhang, L., Amiro, B., Ammann, C., Arain, M.A., Ardö, J., Arkebauer, T., Arndt, S.K., Arriga, N., Aubinet, M., Aurela, M., Baldocchi, D., Barr, A., Beamesderfer, E., Marchesini, L.B., Bergeron, O., Beringer, J., Bernhofer, C., Berveiller, D., Billesbach, D., Black, T.A., Blanken, P.D., Bohrer, G., Boike, J., Bolstad, P.V., Bonal, D., Bonnefond, J.M., Bowling, D.R., Bracho, R., Brodeur, J., Brümmer, C., Buchmann, N., Burban, B., Burns, S.P., Buysse, P., Cale, P., Cavagna, M., Cellier, P., Chen, S., Chini, I., Christensen, T.R., Cleverly, J., Collalti, A., Consalvo, C., Cook, B.D., Cook, D., Coursolle, C., Cremonese, E., Curtis, P.S., D'Andrea, E., da Rocha, H., Dai, X., Davis, K.J., De Cinti, B., de Grandcourt, A., De Ligne, A., De Oliveira, R.C., Delpierre, N., Desai, A.R., Di Bella, C. M., di Tommasi, P., Dolman, H., Domingo, F., Dong, G., Dore, S., Duce, P., Dufrêne, E., Dunn, A., Dušek, J., Eamus, D., Eichelmann, U., ElKhidir, H.A.M., Eugster, W., Ewenz, C.M., Ewers, B., Famulari, D., Fares, S., Feigenwinter, I., Feitz, A., Fensholt, R., Filippa, G., Fischer, M., Frank, J., Galvagno, M., Gharun, M., Gianelle, D., Gielen, B., Gioli, B., Gitelson, A., Goded, I., Goeckede, M., Goldstein, A. H., Gough, C.M., Goulden, M.L., Graf, A., Griebel, A., Gruening, C., Grünwald, T., Hammerle, A., Han, S., Han, X., Hansen, B.U., Hanson, C., Hatakka, J., He, Y., Hehn, M., Heinesch, B., Hinko-Najera, N., Hörtnagl, L., Hutley, L., Ibrom, A., Ikawa, H., Jackowicz-Korczynski, M., Janouš, D., Jans, W., Jassal, R., Jiang, S., Kato, T., Khomik, M., Klatt, J., Knohl, A., Knox, S., Kobayashi, H., Koerber, G., Kolle, O., Kosugi, Y., Kotani, A., Kowalski, A., Kruijt, B., Kurbatova, J., Kutsch, W.L., Kwon, H., Launiainen, S., Laurila, T., Law, B., Leuning, R., Li, Yingnian, Liddell, M., Limousin, J.M., Lion, M., Liska, A.J., Lohila, A., López-Ballesteros, A., López-Blanco, E., Loubet, B., Loustau, D., Lucas-Moffat, A., Lüers, J., Ma, S., Macfarlane, C., Magliulo, V., Maier, R., Mammarella, I., Manca, G., Marcolla, B., Margolis, H.A., Marras, S., Massman, W., Mastepanov, M., Matamala, R., Matthes, J.H., Mazzenga, F., McCaughey, H., McHugh, I., McMillan, A.M.S., Merbold, L., Meyer, W., Meyers, T., Miller, S.D., Minerbi, S., Moderow, U., Monson, R.K., Montagnani, L., Moore, C.E., Moors, E., Moreaux, V., Moureaux, C., Munger, J.W., Nakai, T., Neirynck, J., Nesic, Z., Nicolini, G., Noormets, A., Northwood, M., Nosetto, M., Nouvellon, Y., Novick, K., Oechel, W., Olesen, J.E., Ourcival, J.M., Papuga, S.A., Parmentier, F.J., Paul-Limoges, E., Pavelka, M., Peichl, M., Pendall, E., Phillips, R.P., Pilegaard, K., Pirk, N., Posse, G., Powell, T., Prasse, H., Prober, S.M., Rambal, S., Rannik, Ü., Raz-Yaseef, N., Reed, D., de Dios, V.R., Restrepo-Coupe, N., Reverter, B.R., Roland, M., Sabbatini, S., Sachs, T., Saleska, S.R., Sánchez-Cañete, E. P., Sanchez-Mejia, Z.M., Schmid, H.P., Schmidt, M., Schneider, K., Schrader, F., Schroder, I., Scott, R.L., Sedlák, P., Serrano-Ortíz, P., Shao, C., Shi, P., Shironya, I., Siebicke, L., Šigut, L., Silberstein, R., Sirca, C., Spano, D., Steinbrecher, R., Stevens, R.M., Sturtevant, C., Suyker, A., Tagesson, T., Takanashi, S., Tang, Y., Tapper, N., Thom, J., Tiedemann, F., Tomassucci, M., Tuovinen, J.P., Urbanski, S., Valentini, R., van der Molen, M., van Gorsel, E., van Huissteden, K., Varlagin, A., Verfaillie, J., Vesala, T., Vincke, C., Vitale, D., Vygodskaya, N., Walker, J.P., Walter-Shea, E., Wang, H., Weber, R., Westermann, S., Wille, C., Wofsy, S., Wohlfahrt, G., Wolf, S., Woodgate, W., Li, Yuelin, Zampedri, R., Zhang, J., Zhou, G., Zona, D., Agarwal, D., Biraud, S., Torn, M., Papale, D., 2020. The FLUXNET2015 dataset and the ONEFlux processing pipeline for eddy covariance data. Sci. data 7, 225. https://doi.org/10.1038/s41597-020-0534-3.

Pell, E.J., Schlagnhaufer, C.D., Arteca, R.N., 1997. Ozone-induced oxidative stress: mechanisms of action and reaction. Physiol. Plant. 100, 264–273. https://doi.org/10.1034/j.1399-3054.1997.1000207.x.

Pereira, J.S., Mateus, J.A., Aires, L.M., Pita, G., Pio, C., David, J.S., Andrade, V., Banza, J., David, T.S., Paço, T.A., Rodrigues, A., 2007. Net ecosystem carbon exchange in three contrasting Mediterranean ecosystems - the effect of drought. Biogeosciences 4, 791–802. https://doi.org/10.5194/bg-4-791-2007.

Philip, E., 2002. Effects of low concentrations of SO$_2$ and NO$_X$ on the photosynthetic characteristics of Pongamia pinnata. J. Trop. For. Sci. 14, 474–484.

Putaud, J.P., Pozzoli, L., Pisoni, E., Martins Dos Santos, S., Lagler, F., Lanzani, G., Dal Santo, U., Colette, A., 2021. Impacts of the COVID-19 lockdown on air pollution at regional and urban background sites in northern Italy. Atmos. Chem. Phys. 21, 7597–7609. https://doi.org/10.5194/acp-21-7597-2021.

Qu, Z., Oumbe, A., Blanc, P., Espinar, B., Gesell, G., Gschwind, B., Klüser, L., Lefèvre, M., Saboret, L., Schroedter-Homscheidt, M., Wald, L., 2017. Fast radiative transfer parameterisation for assessing the surface solar irradiance: The Heliosat-4 method. Meteorol. Zeitschrift 26, 33–57. https://doi.org/10.1127/metz/2016/0781.

Reichstein, M., Falge, E., Baldocchi, D., Papale, D., Aubinet, M., Berbigier, P., Bernhofer, C., Buchmann, N., Gilmanov, T., Granier, A., Grünwald, T., Havránková, K., Ilvesniemi, H., Janous, D., Knohl, A., Laurila, T., Lohila, A., Loustau, D., Matteucci, G., Meyers, T., Miglietta, F., Ourcival, J.M., Pumpanen, J., Rambal, S., Rotenberg, E., Sanz, M., Tenhunen, J., Seufert, G., Vaccari, F., Vesala, T., Yakir, D., Valentini, R., 2005. On the separation of net ecosystem exchange into assimilation and ecosystem respiration: review and improved algorithm. Glob. Chang. Biol. 11, 1424–1439. https://doi.org/10.1111/j.1365-2486.2005.001002.x.

Reichstein, M., Stoy, P.C., Desai, A.R., Lasslop, G., Richardson, A.D., 2012. Partitioning of net fluxes. In: Aubinet, M., Vesala, T., Papale, D. (Eds.), Eddy Covariance. Springer, Dordrecht. https://doi.org/10.1007/978-94-007-2351-1_9.

Roderick, M.L., Farquhar, G.D., Berry, S.L., Noble, I.R., 2001. On the direct effect of clouds and atmospheric particles on the productivity and structure of vegetation. Oecologia 129, 21–30. https://doi.org/10.1007/s004420100760.

Schroedter-Homscheidt, M., Azam, F., Betcke, J., Hoyer-Klick, C., Lefèvre, M., Saint-Drenan, Y.-M., Wey, E., Saboret, L., 2021. User's Guide to the CAMS Radiation Service (CRS): Status December 2021 (Copernicus Atmosphere Monitoring Service).

Schuldt, B., Buras, A., Arend, M., Vitasse, Y., Beierkuhnlein, C., Damm, A., Gharun, M., Grams, T.E.E., Hauck, M., Hajek, P., Hartmann, H., Hiltbrunner, E., Hoch, G., Holloway-Phillips, M., Körner, C., Larysch, E., Lübbe, T., Nelson, D.B., Rammig, A., Rigling, A., Rose, L., Ruehr, N.K., Schumann, K., Weiser, F., Werner, C., Wohlgemuth, T., Zang, C.S., Kahmen, A., 2020. A first assessment of the impact of the extreme 2018 summer drought on central European forests. Basic Appl. Ecol. 45, 86–103. https://doi.org/10.1016/j.baae.2020.04.003.

Sciare, J., D'Argouges, O., Zhang, Q.J., Sarda-Estève, R., Gaimoz, C., Gros, V., Beekmann, M., Sanchez, O., 2010. Comparison between simulated and observed chemical composition of fine aerosols in Paris (France) during springtime: contribution of regional versus continental emissions. Atmos. Chem. Phys. 10, 11987–12004. https://doi.org/10.5194/acp-10-11987-2010.

Tang, A.C.I., Stoy, P.C., Hirata, R., Musin, K.K., Aeries, E.B., Wenceslaus, J., Melling, L., 2018. Eddy covariance measurements of methane flux at a tropical peat forest in Sarawak, Malaysian Borneo. Geophys. Res. Lett. 45, 4390–4399. https://doi.org/10.1029/2017GL076457.

Venter, Z.S., Aunan, K., Chowdhury, S., Lelieveld, J., 2020. COVID-19 lockdowns cause global air pollution declines. Proc. Natl. Acad. Sci. 117, 18984–18990. https://doi.org/10.1073/pnas.2006853117.

Viatte, C., Petit, J.E., Yamanouchi, S., Van Damme, M., Doucerain, C., Germain-Piaulenne, E., Gros, V., Favez, O., Clarisse, L., Coheur, P.F., Strong, K., Clerbaux, C., 2021. Ammonia and PM$_{2.5}$ air pollution in Paris during the 2020 COVID lockdown. Atmosphere 12, 160. https://doi.org/10.3390/atmos12020160.

Voigt, C., Lelieveld, J., Schlager, H., Schneider, J., Curtius, J., Meerkötter, R., Sauer, D., Bugliaro, L., Bohn, B., Crowley, J.N., Erbertseder, T., Groß, S., Hahn, V., Li, Q., Mertens, M., Pöhlker, M., Pozzer, A., Schumann, U., Tomsche, L., Williams, J., Zahn, A., Andreae, M., Borrmann, S., Bräuer, T., Dörich, R., Dörnbrack, A., Edtbauer, A., Ernle, L., Fischer, H., Giez, A., Granzin, M., Grewe, V., Harder, H., Heinritzi, M., Holanda, B.A., Jöckel, P., Kaiser, K., Krüger, O.O., Lucke, J., Marsing, A., Martin, A., Matthes, S., Pöhlker, C., Pöschl, U., Reifenberg, S., Ringsdorf, A., Scheibe, M., Tadic, I., Zauner-Wieczorek, M., Henke, R., Rapp, M., 2022. Cleaner skies during the COVID-19 lockdown. Bull. Am. Meteorol. Soc. 103, E1796–E1827. https://doi.org/10.1175/BAMS-D-21-0012.1.

Wang, X., Wu, J., Chen, M., Xu, X., Wang, Z., Wang, B., Wang, C., Piao, S., Lin, W., Miao, G., Deng, M., Qiao, C., Wang, J., Xu, S., Liu, L., 2018. Field evidences for the positive effects of aerosols on tree growth. Glob. Chang. Biol. 24, 4983–4992. https://doi.org/10.1111/gcb.14339.

Wang, Y., Okochi, H., Igawa, M., 2023. Long term trends of dry and wet deposition of air pollutants at declining forest site of Mt. Oyama in Japan during 1994–2019. Water Air Soil Pollut. 234 https://doi.org/10.1007/s11270-023-06270-3.

Warm Winter 2020 Team & ICOS Ecosystem Thematic Centre, 2022. Warm Winter 2020 ecosystem eddy covariance flux product for 73 stations in FLUXNET-Archive format—release 2022–1 (Version 1.0). ICOS Carbon Portal. URL doi:10.18160/2G60-ZHAK.

Wittig, V.E., Ainsworth, E.A., Naidu, S.L., Karnosky, D.F., Long, S.P., 2009. Quantifying the impact of current and future tropospheric ozone on tree biomass, growth, physiology and biochemistry: a quantitative meta-analysis. Glob. Chang. Biol. 15, 396–424. https://doi.org/10.1111/j.1365-2486.2008.01774.x.

World Health Organisation, 2020. WHO Director-General's opening remarks at the media briefing on COVID-19 - 13 march 2020. https://www.who.int/director-general/speeches/detail/who-director-general-s-opening-remarks-at-the-mission-briefing-on-covid-19---13-march-2020.

Xie, J., Kneubühler, M., Garonna, I., Notarnicola, C., De Gregorio, L., De Jong, R., Chimani, B., Schaepman, M.E., 2017. Altitude-dependent influence of snow cover on

alpine land surface phenology. J. Geophys. Res. Biogeosci. 122, 1107–1122. https://doi.org/10.1002/2016JG003728.

Yu, X., Orth, R., Reichstein, M., Bahn, M., Klosterhalfen, A., Knohl, A., Koebsch, F., 2022. Contrasting drought legacy effects on gross primary productivity in a mixed versus pure beech forest. Biogeosciences 19, 4315–4329.

Zhao, M., Running, S.W., 2010. Drought-induced reduction in global terrestrial net primary production from 2000 through 2009. Science 329, 940–943. https://doi.org/10.1126/science.334.6062.1496.